

# Topological Principles of Borosilicate Glass Chemistry

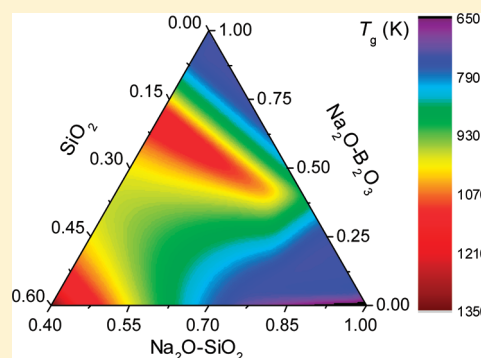
Morten M. Smedskjaer,<sup>†</sup> John C. Mauro,<sup>\*,†</sup> Randall E. Youngman,<sup>†</sup> Carrie L. Hogue,<sup>†</sup> Marcel Potuzak,<sup>†</sup> and Yuanzheng Yue<sup>‡,§</sup>

<sup>†</sup>Science and Technology Division, Corning Incorporated, Corning, New York 14831, United States

<sup>\*</sup>Section of Chemistry, Aalborg University, DK-9000 Aalborg, Denmark

<sup>§</sup>Shandong Key Laboratory for Glass and Ceramics, Shandong Polytechnic University, Jinan 250353, China

**ABSTRACT:** Borosilicate glasses display a rich complexity of chemical behavior depending on the details of their composition and thermal history. Noted for their high chemical durability and thermal shock resistance, borosilicate glasses have found a variety of important uses from common household and laboratory glassware to high-tech applications such as liquid crystal displays. In this paper, we investigate the topological principles of borosilicate glass chemistry covering the extremes from pure borate to pure silicate end members. Based on NMR measurements, we present a two-state statistical mechanical model of boron speciation in which addition of network modifiers leads to a competition between the formation of nonbridging oxygen and the conversion of boron from trigonal to tetrahedral configuration. Using this model, we derive a detailed topological representation of alkali–alkaline earth–borosilicate glasses that enables the accurate prediction of properties such as glass transition temperature, liquid fragility, and hardness. The modeling approach enables an understanding of the microscopic mechanisms governing macroscopic properties. The implications of the glass topology are discussed in terms of both the temperature and thermal history dependence of the atomic bond constraints and the influence on relaxation behavior. We also observe a nonlinear evolution of the jump in isobaric heat capacity at the glass transition when substituting  $\text{SiO}_2$  for  $\text{B}_2\text{O}_3$ , which can be accurately predicted using a combined topological and thermodynamic modeling approach.



## I. INTRODUCTION

Glasses based on silica ( $\text{SiO}_2$ ), boric oxide ( $\text{B}_2\text{O}_3$ ), or a combination thereof play an important role in many technologies. Soda lime silicate ( $\text{Na}_2\text{O}$ – $\text{CaO}$ – $\text{SiO}_2$ ) glasses have been particularly well studied since this glass system forms the basis for a wide range of commercially important products, including architectural windows and glass containers.<sup>1</sup> Nevertheless, the composition of commercial soda lime silicate glass has changed only slightly since its original development by Venetian glass-makers in the 14th century.<sup>2</sup> In the early 19th century, Michael Faraday invented borosilicate glass by demonstrating that a lead borosilicate system could be applied as flint glass.<sup>3</sup> In borosilicate glasses, the mixing of silicon and boron structural units can be used to control and design the physical and chemical properties of these glasses. For example, alkali borosilicates have been applied as thermal shock-resistant glasses (e.g., Pyrex), whereas alkaline earth borosilicate glasses are used as substrate glasses for liquid crystal displays (e.g., EAGLE XG).<sup>4</sup> In contrast, pure borate glasses (i.e., without the addition of silica) have only found limited applications due to their poor chemical durability. Recently, however, it has been discovered that borate glass nanofibers are bioactive and promote the healing of flesh wounds.<sup>5</sup> In these bioactive glasses, the poor chemical durability of the borate glass is an advantage since it promotes soft-tissue regeneration and has an antimicrobial effect.

The structural foundation of borate and borosilicate glass properties is especially interesting owing to the so-called “boron anomaly”,<sup>1,6</sup> in which the initial addition of network modifier ions (i.e., alkali or alkaline earth ions) affects properties differently compared to further additions of these same modifiers.<sup>7–10</sup> For example, the initial incorporation of alkali or alkaline earth ions into a borate or borosilicate glass results in a decrease of the thermal expansion coefficient and an increase in glass transition temperature. However, after a certain concentration of network modifiers is reached, further addition of modifier ions produces the opposite trend, viz., higher thermal expansion coefficient and lower glass transition temperature.<sup>7</sup>

A significant number of studies have been devoted to understanding the structural origin of the boron anomaly in both borate and borosilicate glasses, including both experimental<sup>11–20</sup> and simulation studies.<sup>21–25</sup> In particular, <sup>11</sup>B magic-angle spinning (MAS) nuclear magnetic resonance (NMR) spectroscopy has been applied to study the short-range structure, which provides accurate quantitative data on the coordination state of boron. Such measurements have revealed that the boron anomaly is the result of conversion of boron between threefold-coordinated (trigonal) and fourfold-coordinated (tetrahedral) structural motifs. <sup>11</sup>B NMR was first used by Bray et al. to study boron speciation in pure  $\text{B}_2\text{O}_3$ , alkali

Received: September 12, 2011

Published: September 27, 2011

borate, and borosilicate glasses,<sup>26,27</sup> and later their studies led to the development of structural models for sodium borosilicate glasses.<sup>11,13</sup> Although these structural models can accurately capture the boron speciation in various borosilicate glasses, more recent investigations<sup>17</sup> indicate that alkali ions are more randomly distributed between the silicate and borate structural units compared to what was assumed in these earlier modeling efforts.<sup>11,13</sup> Moreover, NMR studies of borosilicate glass fibers have shown that thermal history plays an important role in determining the boron speciation, with trigonal boron being more favorable at higher fictive temperatures and converting to a tetrahedral configuration upon annealing.<sup>28–30</sup> It is therefore necessary to develop more accurate microscopic models for borosilicate glasses to account for these phenomena.

The computational design of new borosilicate glasses through molecular dynamics simulations is currently impractical owing to the long time scales involved in accounting for a realistic glass transition.<sup>31</sup> Furthermore, the conversion of boron from threefold to fourfold coordination poses a distinct challenge for classical interatomic potentials, even though some progress has very recently been reported.<sup>32</sup> To circumvent these problems, an alternative approach based on the topology of the glass network and the temperature dependence of the bond constraints can be used, assuming that sufficient information is known regarding the connectivity of the network and the hierarchy of constraints.<sup>33–36</sup> For example, Kerner and Phillips<sup>2,37</sup> have recently shown that topological modeling can be used to predict the optimum glass-forming composition of soda lime silicate glass within 1 mol %. This remarkable discovery was made based on simple counting arguments without any adjustable fitting parameters. While the work of Kerner and Phillips followed the empirical discovery of optimal soda lime silicate by several hundred years, which shows how difficult are the structural problems posed by network glasses, their elegant solution points to the exciting prospects of designing new glass compositions from simple topological considerations.

Topological constraint theory of glass was originally developed by Phillips and Thorpe.<sup>38–40</sup> According to this approach, each atom in a glass has three translational degrees of freedom (in a three-dimensional space), which can be removed by the presence of rigid bond constraints, such as two-body radial and three-body angular bond constraints. Depending on the relative difference between the network dimensionality ( $d$ ) and the average number of constraints per atom ( $n$ ), the network can be floppy ( $n < d$ ), isostatic ( $n = d$ ), or stressed rigid ( $n > d$ ). Since the introduction of this theory, it has been extensively used to explain the structural origin of changes in the thermal and mechanical properties of network glasses, and in particular the covalently bonded families of chalcogenide glass.<sup>36,41–49</sup>

In the original theory of Phillips and Thorpe, constraint counting is performed at zero temperature; i.e., all bond constraints are assumed to be intact. More recently, Gupta and Mauro generalized the approach by including an explicit temperature dependence of the constraints.<sup>33,34,36</sup> With increasing temperature, there is more thermal energy available to overcome the activation barrier associated with a given constraint. Hence, a larger fraction of floppy modes becomes available with increasing temperature. Evidence for temperature-dependent constraint theory has been reported from both experiments and molecular dynamics simulations.<sup>47,49,50</sup> For example, Gjersing et al.<sup>47</sup> found evidence for a rigid-to-floppy transition in germanium selenide glasses using <sup>77</sup>Se NMR spectroscopy at high temperatures. The recent molecular dynamics simulations of Bauchy and Micouaut<sup>50</sup> have confirmed the existence of temperature-dependent

constraints in a sodium disilicate glass and verified the analytical functional form used by Mauro et al.<sup>34</sup> for the temperature dependence of the constraints.

The Gupta–Mauro temperature-dependent constraint theory provides quantitatively accurate calculations of macroscopic properties such as the glass transition temperature ( $T_g$ ), liquid fragility index ( $m$ ), and Vickers hardness ( $H_V$ ).<sup>9,33–35,51</sup> This topological modeling approach involves three basic steps: (i) identification and counting of the number of distinct network species as a function of composition; (ii) identification and counting of the number of constraints associated with each species; and (iii) ranking the constraints in terms of their relative onset temperatures, where a higher onset temperature indicates a higher activation barrier to break the constraint. The property calculations are then performed by connecting the change in the topological degrees of freedom ( $f = d - n$ ) with a change in the specific property of interest. For example, Naumis has shown that  $f$  is proportional to the configurational entropy ( $S_c$ ) of the system.<sup>46,52</sup> When substituted into the Adam–Gibbs relation,<sup>53</sup> the viscosity ( $\eta$ ) can then be calculated.<sup>54</sup> Hence,  $T_g$  and  $m$  can be calculated as a function of composition, as explained in more detail in sections III.C and III.D, respectively. This approach for calculating the composition dependence of glass properties has been successfully applied to germanium selenide,<sup>33</sup> alkali borate,<sup>34</sup> and alkali–alkaline earth–borate<sup>9,35</sup> systems. Here, we extend the approach for the first time to a quaternary glass system with multiple network formers, viz., the alkali–alkaline earth–borosilicate system. In order to develop a rigorous topological model for borosilicate glasses, we must first account accurately for the change in boron and silicon speciation with composition and temperature and then associate appropriate constraints with each of these species. In addition, the modifying cations can also provide constraints due to clustering,<sup>35</sup> as in the modified random network model of Greaves.<sup>55,56</sup>

In this work, we prepare and study a series of borosilicate glasses with constant modifier content but varying  $[\text{SiO}_2]/[\text{B}_2\text{O}_3]$  ratio, viz.,  $(0.75 - z)\text{SiO}_2 - z\text{B}_2\text{O}_3 - 0.15\text{Na}_2\text{O} - 0.10\text{CaO}$  with  $z = 0, 0.06, 0.12, 0.24, 0.375, 0.51, 0.63$ , and  $0.75$ , since this series contains abundant topological and structural features, e.g., the boron anomaly. The structure of the glasses is analyzed using <sup>11</sup>B and <sup>29</sup>Si MAS NMR spectroscopy. In order to describe the composition dependence of boron speciation, we propose a two-state statistical mechanical model and compare it to previous models. The two-state model is developed in a way to account naturally for the dependence of boron speciation on thermal history (i.e., fictive temperature). Using the topological principles, we accurately predict the glass transition temperature, the liquid fragility index, and the hardness of the annealed glasses at room temperature. In each case, we demonstrate good quantitative agreement with the experimental data. We also investigate how the heat capacity jump during the glass transition changes when substituting  $\text{SiO}_2$  for  $\text{B}_2\text{O}_3$ , and we propose a model to account for this change. Furthermore, we discuss how the topological modeling approach can be applied both for understanding the microstructural and topological origins of macroscopic properties and for the quantitative design of new borosilicate glass compositions with desired properties.

## II. STRUCTURE AND GLASS TRANSITION BEHAVIOR

**A. Sample Preparation.** The series of borosilicate glasses was synthesized using analytical reagent-grade  $\text{H}_3\text{BO}_3$  (Sigma-Aldrich,  $\geq 99.5\%$ ),  $\text{SiO}_2$  (Sigma-Aldrich, purum p.a.),  $\text{Na}_2\text{CO}_3$  (Merck,  $\geq 99.9\%$ ), and  $\text{CaCO}_3$  (Merck,  $\geq 99.5\%$ ) powders. The thoroughly mixed batches were melted and homogenized in a

Table 1. Analyzed Compositions and Properties of the Investigated Glass Samples<sup>a</sup>

glass ID	chemical composition (mol %)				$N_4$ (atom %)	$Q_4$ (atom %)	$T_g$ (K)	$m$ (—)	$\Delta C_p$ (J mol <sup>-1</sup> K <sup>-1</sup> )	$H_V$ (GPa)
	SiO <sub>2</sub>	B <sub>2</sub> O <sub>3</sub>	Na <sub>2</sub> O	CaO						
75B	0.0	74.1	15.4	10.5	39.9	n/a	775	54 ± 3	50.8	7.6 ± 0.2
63B–12Si	12.7	62.0	14.9	10.4	45.3	27	790	51 ± 2	51.9	8.6 ± 0.2
51B–24Si	24.9	49.3	15.0	10.8	48.9	33	803	50 ± 5	51.0	9.3 ± 0.3
37B–37Si	36.9	38.4	14.1	10.6	53.5	28	813	50 ± 3	49.1	9.6 ± 0.2
24B–51Si	51.6	21.9	15.5	11.0	65.5	37	833	48 ± 6	41.7	10.0 ± 0.3
12B–63Si	63.8	10.8	14.8	10.6	75.8	31	842	42 ± 4	29.3	10.1 ± 0.2
6B–69Si	69.3	4.9	16.1	9.8	80.8	26	837	39 ± 3	25.2	9.8 ± 0.3
75Si	74.8	0.0	15.2	10.1	n/a	28	814	30 ± 5	16.4	9.2 ± 0.4

<sup>a</sup> The fractions of four-coordinated boron ( $N_4$ ) and silicon with four bridging oxygens ( $Q_4$ ) have been determined using <sup>11</sup>B and <sup>29</sup>Si MAS NMR spectroscopy, respectively. The glass transition temperature ( $T_g$ ) and the jump in heat capacity ( $\Delta C_p = C_{pl} - C_{pg}$ ) have been determined using DSC at a heating/cooling rate of 10 K/min. The error in  $T_g$  associated with this method is generally 2–3 K. The liquid fragility index ( $m$ ) has been determined by performing DSC measurements at different heating/cooling rates. The glass hardness ( $H_V$ ) has been measured by the Vickers microindentation test at a load of 0.25 N.

covered Pt<sub>90</sub>Rh<sub>10</sub> crucible at a temperature  $T_h$  in an inductively heated furnace.  $T_h$  was varied between 1100 and 1500 °C and the melting time varied between 1 and 3 h depending on the level of silica. Melting in an induction furnace helps to enhance melt homogeneity and minimize boron evaporation. Chemical composition analysis using wet chemistry shows that the glasses are within 1–2 mol % of the desired compositions (see Table 1). The glasses were annealed for 2–2.5 h at their respective  $T_g$  (see section II.C). All samples were kept in glass or plastic containers with desiccant. There was no evidence of phase separation in these glasses.

**B. Glass Network Structure.** Glassy SiO<sub>2</sub> consists of corner-sharing SiO<sub>4</sub> tetrahedra with bridging oxygens (BO) linking to neighboring Si atoms, which lacks long-range order. Addition of network-modifying alkali or alkaline earth oxide to SiO<sub>2</sub> results in a creation of nonbridging oxygens (NBOs) by breaking the linkages between SiO<sub>4</sub> tetrahedra.<sup>1</sup> The ratio of silicon atoms with  $j$  number of BOs to the total silicon atoms is denoted as

$$Q_j = \frac{c(Q^j)}{\sum_{j=0}^4 c(Q^j)} \quad (1)$$

where  $c(Q^j)$  is the number of silicon units with  $j$  bridging oxygens.

Glassy B<sub>2</sub>O<sub>3</sub> consists of corner-sharing BO<sub>3</sub> triangles ( $B^3$ ), a large fraction of which combine to form three-membered boroxol ring units.<sup>57–60</sup> Upon addition of alkali or alkaline earth oxide to B<sub>2</sub>O<sub>3</sub>, there are two possibilities: (a) creation of a NBO, rupturing the linkage between two trigonally coordinated  $B^3$  groups, or (b) conversion of boron from three-coordinated (trigonal boron,  $B^3$ ) to a four-coordinated (tetrahedral boron,  $B^4$ ) state without the creation of a NBO.<sup>1</sup> The random pair model of Gupta<sup>61</sup> establishes three rules for network formation: (1)  $B^4$  tetrahedra occur in corner-sharing pairs, i.e., there is one  $B^4$ –O– $B^4$  bridge for every pair, and the  $B^4$ –O– $B^4$  angle within a pair is random; (2) pairs of  $B^4$  tetrahedra cannot be bound to each other; and (3) NBOs occur only in  $B^3$  groups and not in  $B^4$  groups. The fraction of tetrahedral to total boron ( $N_4$ ) is expressed as

$$N_4 = \frac{c(B^4)}{c(B^3) + c(B^4)} \quad (2)$$

where  $c(B^3)$  and  $c(B^4)$  are the number of three- and four-coordinated boron units, respectively. In pure borate glasses, the

maximum value of  $N_4$  is 50%, as dictated by the random pair model. In borosilicate glasses, the silicate and borate groups mix, allowing  $N_4$  to exceed 50%. However, the degree of Si/B mixing and distribution of the network-modifying cations have been intensively debated.<sup>11,13,17,19,20,62–65</sup> Here, we use <sup>11</sup>B and <sup>29</sup>Si MAS NMR to elucidate the structure of the borosilicate glasses.

**Experimental Procedure.** <sup>11</sup>B and <sup>29</sup>Si MAS NMR experiments were performed to determine the local network structure as the silicate glass network gradually converts into a borate glass network with increasing  $z$ . <sup>11</sup>B MAS NMR experiments were conducted at 11.7 T (160.34 MHz resonance frequency) using a commercial spectrometer (VNMRs, Agilent) and a commercial 3.2 mm MAS NMR probe (Varian/Chemagnetics). Powdered glasses were packed into 3.2 mm zirconia rotors with sample spinning at 20 kHz. Radio frequency pulses (0.6  $\mu$ s), corresponding to a  $\pi/12$  tip angle, were used to uniformly excite the <sup>11</sup>B central transitions and thus provide quantitatively accurate B speciation. The <sup>11</sup>B MAS NMR spectra were processed without additional line broadening and referenced using aqueous boric acid at 19.6 ppm relative to the conventional shift reference (BF<sub>3</sub>–Et<sub>2</sub>O). <sup>29</sup>Si MAS NMR measurements were performed at 4.7 T (30.38 MHz resonance frequency) with a commercial spectrometer (Varian/Chemagnetics Infinity) and a 7.5 mm MAS NMR probe (Varian/Chemagnetics). Powdered glasses were loaded into 7.5 mm zirconia rotors for sample spinning at 4 kHz. <sup>29</sup>Si MAS NMR data were collected using  $\pi/6$  tip angles (1.7  $\mu$ s) and recycle delays of 180 s. Several additional measurements using longer delays to account for differential relaxation of the <sup>29</sup>Si nuclei confirmed these parameters were sufficient for accurate determination of the <sup>29</sup>Si MAS NMR spectra. Five hundred to two thousand scans were coadded and processed using approximately 1 ppm of line broadening (39 Hz) and referenced to an external tetramethylsilane standard at 0.0 ppm.

<sup>29</sup>Si and <sup>11</sup>B MAS NMR spectra were analyzed using the Dmfit program.<sup>66</sup> The <sup>29</sup>Si spectra were fit using a sum of two Gaussian line shapes, where the widths of these peaks were constrained to the values obtained for the B-free glass. <sup>11</sup>B MAS NMR line shapes were simulated using one or two trigonal peaks with second-order quadrupolar effects and a single mixed Gaussian/Lorentzian peak for the tetrahedral B resonance. Peak intensities were obtained by numerical integration of the various simulated line shapes.

**Results.** Figure 1a shows the <sup>11</sup>B MAS NMR spectra for the B-containing glasses. The spectra contain two types of <sup>11</sup>B resonances, a complicated line shape between 5 and 20 ppm



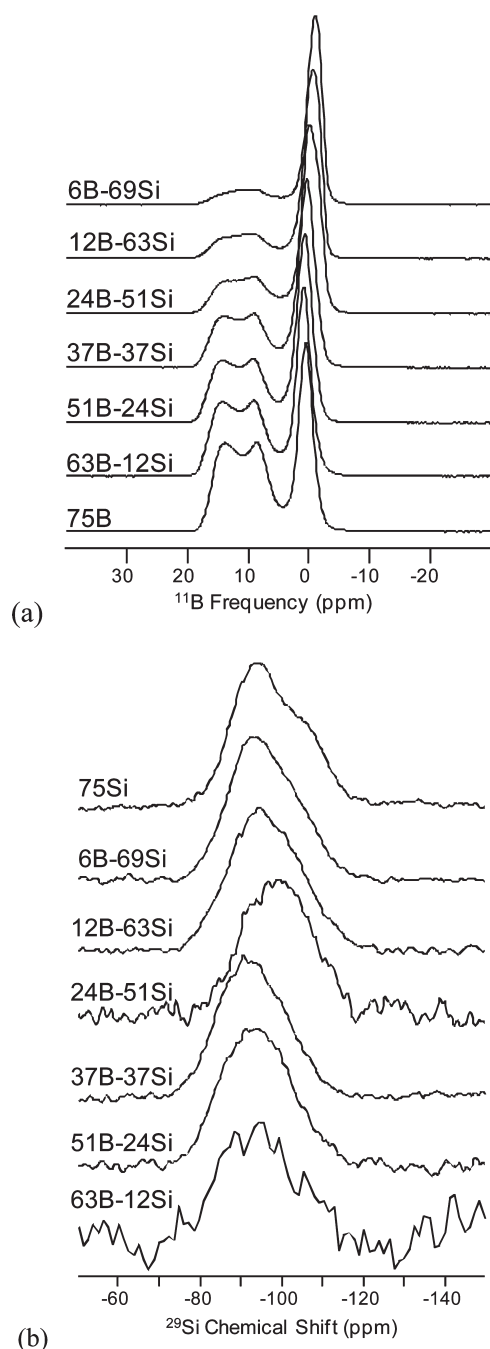


**Figure 1.** MAS NMR spectra of (a) boron-11 and (b) silicon-29 for the borosilicate glasses. The intensity of each spectrum is normalized to that of its most intense peak. Glass IDs (Table 1) are denoted to the left of these spectra.

due to trigonal boron and a relatively narrow resonance near 0 ppm from tetrahedral boron. The large differences in peak shape reflect the presence or absence of second-order quadrupolar interactions, which arise from symmetry around the boron atom. In the case of trigonal boron, these interactions are still present and cannot be averaged away with simple MAS NMR, leading to the complex line shapes in Figure 1a. However, under these experimental conditions, the high symmetry around tetrahedral boron units leads to a very weak quadrupolar coupling and hence a much narrower peak. We obtain the  $N_4$  value by integration of the  $B^4$  and  $B^3$  simulated peaks and find that  $N_4$  increases with decreasing

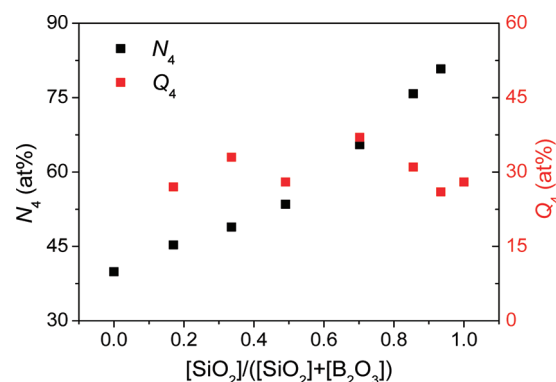


**Figure 2.** Composition dependence of  $N_4$  and  $Q_4$  obtained from the  $^{11}\text{B}$  and  $^{29}\text{Si}$  MAS NMR spectra in Figure 1.  $N_4$  is the fraction of tetrahedral to total boron (eq 2).  $Q_4$  is the ratio of silicon atoms with four BOs to total silicon (eq 1).

$\text{B}_2\text{O}_3$  concentration,  $z$  (Table 1 and Figure 2). There are also distinct changes in peak position for the tetrahedral boron resonance, reflecting perhaps a change in second-nearest neighbor cation distribution (i.e., B and Si) on going from boron-rich to silica-rich glasses. We also detect changes in the trigonal boron line shape with  $z$ , consistent with a second trigonal boron environment having at least one NBO for glasses where  $[\text{SiO}_2] > [\text{B}_2\text{O}_3]$ . These additional structural details, as well as examination of the sodium environments, are beyond the scope of this work and will be presented elsewhere.

Figure 1b contains the  $^{29}\text{Si}$  MAS NMR spectra of the Si-containing glasses. There are subtle changes in the line shape and chemical shift as a function of  $z$ , although the spectra are mostly similar in that they appear to contain two broad and overlapping peaks from at least two types of silicate polyhedra. Formation of NBO and the resulting depolymerization of the silicate network is reflected in a general increase in  $^{29}\text{Si}$  chemical shift as  $Q^4$  groups are converted to  $Q^3$  units. This is most apparent in the spectrum of the boron-free glass (top spectrum of Figure 1b), which contains two resonances at  $-94$  and  $-105$  ppm, assigned to  $Q^3$  and  $Q^4$  groups, respectively. A simple Gaussian fit to these spectra allows for the determination of  $Q^3$  and  $Q^4$  populations (see Table 1 and Figure 2). We fit all these spectra using only two resonances and with only a single fitting constraint for each peak (the full width at half-maximum (fwhm) is constrained to the values determined using the boron-free glass, which exhibits the highest resolution and signal-to-noise and was very well fit using two Gaussian line shapes). As shown in Figure 2, the values for  $Q_4$  in these glasses, as defined in eq 1, do not vary appreciably with composition, consistent with the overall spectral trends in Figure 1b. As mentioned above for boron, the change in neighboring cations with glass composition may also be a contributing factor in small peak shifts in the  $^{29}\text{Si}$  MAS NMR data—the focus of an ongoing study.

**C. Glass Transition Behavior.** *Experimental Procedure.* The values of  $T_g$ ,  $m$ , and  $\Delta C_p$  were determined using a standard calorimetric method.  $\Delta C_p$  is equal to the difference between  $C_{p,l}$  and  $C_{p,g}$ , where  $C_{p,l}$  and  $C_{p,g}$  are the isobaric heat capacity of the liquid and glass, respectively. The calorimetric measurements were performed with a differential scanning calorimetry (DSC) instrument (STA 449C Jupiter, Netzsch). The measurements were conducted in a purged argon atmosphere (40 mL/min). The isobaric heat capacity ( $C_p$ ) curve for each measurement was calculated relative to the  $C_p$  curve of a sapphire reference material of comparable mass. The samples were subjected to two runs of DSC upscans and downscans. The upscan and downscan rates were set at the scan rate  $q$ , which was

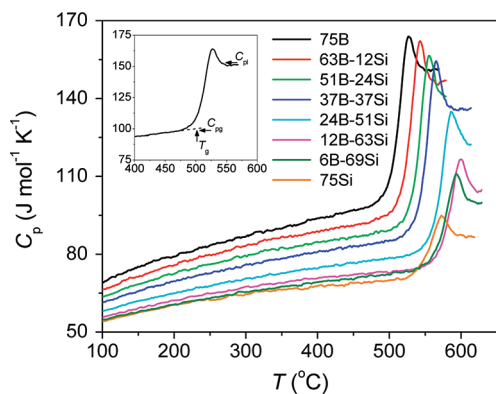


**Figure 3.** Isobaric heat capacity ( $C_p$ ) curves of the eight borosilicate glasses as determined by DSC at a heating rate of 10 K/min subsequent to a cooling procedure at the same rate. The inset illustrates how  $C_{p,g}$  and  $C_{p,l}$  are determined for the 75B glass.

varied between 1 and 30 K/min. The recorded heat flow of the first upscan reflects the enthalpy response of a sample with the initially formed (i.e., unknown) thermal history, whereas that of the second upscan reflects the enthalpy response of the sample with a well-defined thermal history.

**Results.** Figure 3 shows the isobaric heat capacity curves recorded during DSC upscans at 10 K/min for the eight glass compositions. The calorimetric fictive temperature ( $T_f$ ) is defined as the crossing point of the extrapolated straight line of the glass  $C_p$  curve before the transition zone with the tangent at the inflection point of the sharp rise curve of  $C_p$  in the transition zone. For  $q = 10$  K/min,  $T_f$  corresponds to the standard glass transition temperature,  $T_g$ .<sup>67</sup>  $T_g$  first increases and later decreases with increasing  $[\text{SiO}_2]/[\text{B}_2\text{O}_3]$  ratio (Table 1).

The value of  $T_f$  increases with increasing scan rate  $q$ . The dependence of the reciprocal DSC scan rate on  $T_f$  corresponds to the temperature dependence of the equilibrium viscosity. Thus, the  $T_f$  vs  $q$  data can be used to determine the liquid fragility index ( $m$ ).<sup>68</sup> The fragility  $m$  is defined as the slope of the  $\log \eta$  versus  $T_g/T$  curve at  $T_g$ :<sup>69</sup>

$$m \equiv \left. \frac{\partial \log \eta(T)}{\partial (T_g/T)} \right|_{T=T_g} \quad (3)$$

The determined values of  $m$  are given in Table 1. We find that the fragility index decreases monotonically (i.e., the liquids become “stronger”) with increasing  $[\text{SiO}_2]/[\text{B}_2\text{O}_3]$  ratio.

In addition to the observed changes in  $T_g$  and  $m$ , another interesting feature of the DSC curves is the composition dependence of the heat capacity jump during the glass transition. To calculate  $\Delta C_p = C_{p,l} - C_{p,g}$  and  $C_{p,l}/C_{p,g}$ , we determine  $C_{p,l}$  and  $C_{p,g}$  from the DSC upscans (see inset of Figure 3).  $C_{p,l}$  is the offset value of the  $C_p$  overshoot above the glass transition range. A linear function is fitted to the  $C_p$  values at temperatures below  $T_g$  to determine  $C_{p,g}$ . The value of this function at  $T_g$  is reported as  $C_{p,g}$ . Table 1 and Figures 3 and 4 show that  $\Delta C_p$  decreases with increasing  $[\text{SiO}_2]/[\text{B}_2\text{O}_3]$  ratio. Interestingly, this decrease in  $\Delta C_p$  scales nonlinearly with composition, remaining essentially unchanged until the molar  $[\text{SiO}_2]/([\text{SiO}_2] + [\text{B}_2\text{O}_3])$  ratio reaches approximately 0.6 and then decreasing significantly until reaching the final  $\Delta C_p$  value of pure soda lime silicate. We also note that the entire  $C_p$  curves are generally shifted lower with increasing  $[\text{SiO}_2]/[\text{B}_2\text{O}_3]$  ratio (Figure 3).

There have been several attempts to correlate the kinetic fragility index  $m$  with thermodynamic property change at

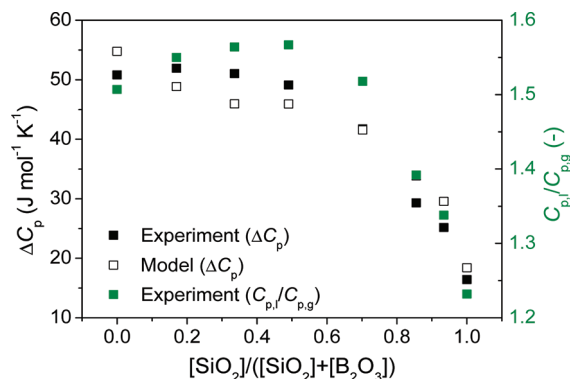


**Figure 4.** Composition dependence of the change in the isobaric heat capacity during the glass transition. The change is quantified by both the ratio and the difference between the liquid ( $C_{p,l}$ ) and glass ( $C_{p,g}$ ) heat capacity. The experimental data are the filled squares, and the model calculations of  $\Delta C_p(x, y, z)$  using eq 10 with  $A = 19$  kJ/mol are the open squares.

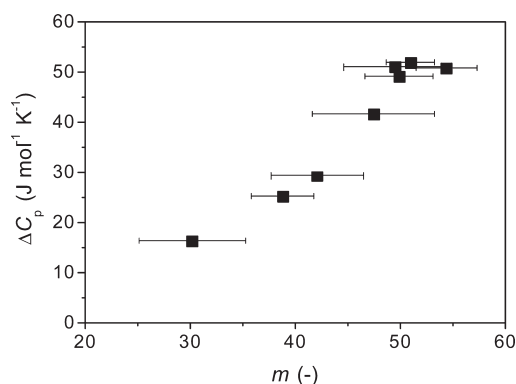


**Figure 5.** Correlation between the change in the isobaric heat capacity during the glass transition ( $\Delta C_p$ ) and the liquid fragility index ( $m$ ) for the eight borosilicate glasses.

$T_g$ .<sup>69–73</sup> For most glass-forming liquids, an increase of  $m$  leads to a corresponding increase of  $\Delta C_p$ ; however, there are notable exceptions to this trend.<sup>69</sup> For the borosilicate liquids studied in this work, we find that the evolution of  $\Delta C_p$  with composition coincides with the change of fragility (Figure 5). However, in the following we propose a more detailed model to understand the origin of the heat capacity jump at the glass transition and to account quantitatively for the composition dependence of  $\Delta C_p$ .

**Model for Composition Dependence of  $\Delta C_p$ .** Our model for  $\Delta C_p(x, y, z)$  of the  $x\text{Na}_2\text{O}-y\text{CaO}-z\text{B}_2\text{O}_3-(1-x-y-z)\text{SiO}_2$  system begins with a discussion about the configurational heat capacity ( $C_{p,\text{conf}}$ ). According to an enthalpy landscape approach, isobaric heat capacity of a glass-forming system is a sum of vibrational and configurational contributions arising from intra- and interbasin transitions, respectively.<sup>74</sup> The interbasin transitions are relatively slow such that upon cooling they begin to freeze, starting with those having the highest activation barriers.<sup>75,76</sup> At the glass transition temperature, the configuration space partitions into a set of metabasins with slow transitions between these metabasins.<sup>77,78</sup> Consequently, the glassy state contains primarily vibrational degrees of freedom, whereas the liquid state contains both vibrational and configurational degrees of freedom. Potuzak et al.<sup>79</sup> have recently provided direct experimental evidence for factoring of the isobaric partition function into separate configurational and vibrational

contributions. However, from calorimetric measurements, a pure configurational heat capacity cannot be directly obtained, but the excess heat capacity  $\Delta C_p$  can be determined, which may contain both vibrational and configurational contributions.<sup>70</sup> According to ref 80 and the references therein, the configurational contribution constitutes the major fraction of the excess entropy, and  $\Delta C_p$  and  $C_{p,\text{conf}}$  are approximately proportional. For relatively strong systems,  $\Delta C_p$  and  $C_{p,\text{conf}}$  are even closer to each other. Since the inorganic systems studied in this work are all relatively strong ( $m = 30\text{--}55$ ), we make the following approximation:

$$\Delta C_p = C_{\text{pl}} - C_{\text{pg}} \approx C_{p,\text{conf}} \quad (4)$$

$C_{p,\text{conf}}$  can be written in terms of configurational enthalpy ( $H_{\text{conf}}$ ) and entropy ( $S_{\text{conf}}$ ):

$$\begin{aligned} \Delta C_p(x, y, z, T) &= \left( \frac{\partial H_{\text{conf}}}{\partial T} \right)_p = \left( \frac{\partial H_{\text{conf}}}{\partial \ln S_{\text{conf}}} \right)_p \left( \frac{\partial \ln S_{\text{conf}}}{\partial T} \right)_p \\ &= \frac{1}{T} \left( \frac{\partial H_{\text{conf}}}{\partial \ln S_{\text{conf}}} \right)_p \left( \frac{\partial \ln S_{\text{conf}}}{\partial \ln T} \right)_p \end{aligned} \quad (5)$$

Building on concepts from previous studies,<sup>70–73</sup> we then derive a correlation between  $\Delta C_p$  and  $m$ . To do so, we first consider the Adam–Gibbs model for equilibrium viscosity<sup>53</sup>

$$\eta = \eta_\infty \exp \left( \frac{B}{TS_{\text{conf}}} \right) \quad (6)$$

where  $\eta_\infty$  is the extrapolated viscosity at infinite temperature and  $B$  is a constant. This equation is interesting in that it connects kinetics ( $\eta$ ) as a function of a thermodynamic variable ( $S_{\text{conf}}$ ). Combining the Adam–Gibbs model with the definition of fragility (eq 3) yields

$$m = m_0 \left( 1 + \frac{\partial \ln S_{\text{conf}}(T)}{\partial \ln T} \right) \bigg|_{T=T_g} \quad (7)$$

where  $m_0 \approx 15\text{--}17$  is the fragility of a strong liquid.<sup>33</sup> Insertion of eq 7 into eq 5 gives

$$\begin{aligned} \Delta C_p[x, y, z, T_g(x, y, z)] &= \frac{1}{T_g(x, y, z)} \left( \frac{\partial H_{\text{conf}}}{\partial \ln S_{\text{conf}}} \right)_{p, T=T_g(x, y, z)} \left( \frac{m(x, y, z)}{m_0} - 1 \right) \end{aligned} \quad (8)$$

which can be rewritten as

$$\begin{aligned} \Delta C_p[x, y, z, T_g(x, y, z)] &= \frac{S_{\text{conf}}[x, y, z, T_g(x, y, z)]}{T_g(x, y, z)} \left( \frac{\partial H_{\text{conf}}}{\partial S_{\text{conf}}} \right)_{p, T=T_g(x, y, z)} \left( \frac{m(x, y, z)}{m_0} - 1 \right) \end{aligned} \quad (9)$$

According to temperature-dependent constraint theory,<sup>33,34</sup>  $S_{\text{conf}}$  at  $T_g$  is inversely proportional to  $T_g$ .  $\partial H_{\text{conf}}/\partial S_{\text{conf}}$  is by definition equal to the configurational temperature ( $T_{\text{conf}}$ ) at constant pressure.<sup>81</sup> For a standard cooling rate, this configurational temperature is equal to the glass transition temperature, i.e.,  $T_{\text{conf}} = T_g$ . Hence, eq 9 can be rewritten as

$$\begin{aligned} \Delta C_p[x, y, z, T_g(x, y, z)] &= \frac{A((x, y, z)_R)}{[T_g(x, y, z)]^2} T_{\text{conf}}(x, y, z) \left( \frac{m(x, y, z)}{m_0} - 1 \right) \\ &= \frac{A((x, y, z)_R)}{T_g(x, y, z)} \left( \frac{m(x, y, z)}{m_0} - 1 \right) \end{aligned} \quad (10)$$

where  $A((x, y, z)_R)$  is the proportionality constant connecting  $S_{\text{conf}}(T_g)$  with  $T_g$  for a reference composition  $(x, y, z)_R$ . Using the measured values of  $T_g$  and  $m$ , we can predict  $\Delta C_p$ , where  $A$  is the scaling factor fit to the experimental data. With the value  $A = 19$  kJ/mol, we find excellent agreement between measured and predicted values of  $\Delta C_p$  (Figure 4). This agreement provides evidence that thermodynamic changes during the glass transition are indeed connected to the kinetic fragility index for the series of glasses with varying  $[\text{SiO}_2]/[\text{B}_2\text{O}_3]$  ratio. This also implies that a direct relation exists between  $\Delta C_p$  and  $C_{p,\text{conf}}$ , which is also subsumed in the scaling factor  $A$ .

**D. Models for Boron Speciation.** To use the topological constraint model for prediction of property values, the composition dependence of the fraction of network-forming species must first be established. For borosilicate glasses, it is therefore essential to capture the proportion of fourfold-coordinated boron atoms,  $N_4$ . The composition dependence of the experimentally determined  $N_4$  values is illustrated in Figure 2. In the following, we attempt to capture this experimental trend using three different models.

The borosilicate glass system is expressed as

$$x\text{Na}_2\text{O} \cdot y\text{CaO} \cdot z\text{B}_2\text{O}_3 \cdot (1 - x - y - z)\text{SiO}_2 \quad (11)$$

We first consider an ideal counting (IC) model, where  $N_4$  is calculated under the following assumptions:

- 1 The effect of one  $\text{Ca}^{2+}$  ion on boron speciation is the same as that of two  $\text{Na}^+$  ions.<sup>8,35,82</sup>
- 2  $\text{B}^4$  units occur in corner-sharing pairs<sup>61</sup> and must be bound only to  $\text{B}^3$  units or  $\text{SiO}_4$  tetrahedra. Hence, the maximum  $\text{B}^4$  fraction is limited by the number of available  $\text{BO}_{3/2}$  and  $\text{SiO}_{4/2}$  bonds.
- 3 Excess  $\text{CaO}$  and  $\text{Na}_2\text{O}$  create NBOs on either the  $\text{B}^3$  or tetrahedral  $\text{SiO}_4$  units.

With the IC model, we can calculate the proportion of fourfold-coordinated boron atoms as

$$N_{4,\text{IC}} = \min \left[ \frac{x + y}{z}, \frac{3 - 7(x + y) + z}{4z}, 1 \right] \quad (12)$$

where the first term in the minimum function applies when the  $\text{B}^4$  fraction is limited by the modifier content, the second term accounts for the case of excess modifier (i.e., NBOs are forming and  $N_4$  is limited by the number of available bonds to  $\text{B}^3$  units and Si tetrahedral, since the pairs of  $\text{B}^4$  groups cannot be bound to each other), and the third term is the upper limit where there is excess modifier and excess number of  $\text{B}^3$  and Si tetrahedral bonds.

Second, we consider the Yun–Bray model<sup>11</sup> with the incorporation of assumption 1 above. According to this model, the concentration of fourfold-coordinated boron increases proportionally with the modifier content up to a maximum and then diminishes, since further modifier addition leads to NBO formation on the silica tetrahedra. The maximum proportion of  $\text{B}^4$  increases with the  $[\text{SiO}_2]/[\text{B}_2\text{O}_3]$  ratio, since it is assumed that threefold-coordinated boron does not mix with the silica network.<sup>13</sup> The formulas for calculating  $N_4$  in the different regimes are given in Table 2.<sup>11</sup>

As shown in Figure 6, the overall trend using both the IC and Yun–Bray models is in good agreement with the  $^{11}\text{B}$  NMR results. However, both of these models predict a saturation of

**Table 2. Formulas for Calculating the Fraction of Four-Coordinated to Total Boron ( $N_4$ ) Following the Structural Model of Yun and Bray for Borosilicate Glasses<sup>11a</sup>**

$K \leq 8, R_{\max} = K/16 + 0.5$		$K \geq 8, R_{\max} = 1$
$R \leq R_{\max}$	$N_4 = R$	$N_4 = R$
$R \geq R_{\max}$	$N_4 = R_{\max} - 0.25(R - R_{\max})/(1 + K)$	$N_4 = 1$

<sup>a</sup>We assume that the effect of one  $\text{Ca}^{2+}$  ion on boron speciation is the same as that of two  $\text{Na}^+$  ions<sup>8,35,82</sup> and set  $R = ([\text{Na}_2\text{O}] + [\text{CaO}])/[\text{B}_2\text{O}_3]$  and  $K = [\text{SiO}_2]/[\text{B}_2\text{O}_3]$ .

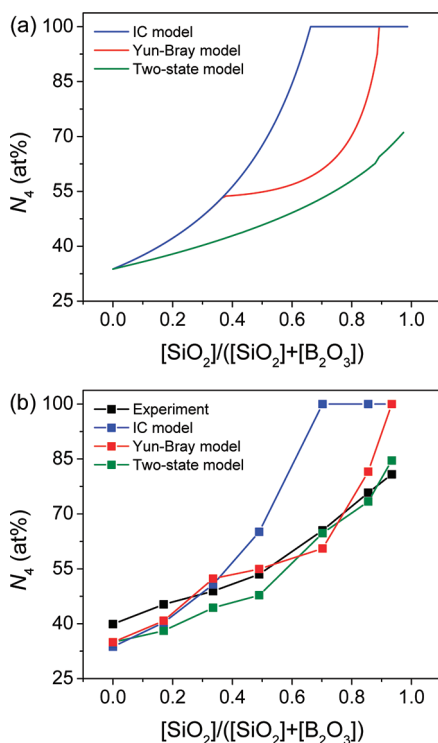


**Figure 6.** Dependence of the fraction of four-coordinated to total boron ( $N_4$ ) on composition using experimental  $^{11}\text{B}$  NMR data and IC (eq 12), Yun–Bray (Table 2), and two-state (eq 15) models. (a) Calculations assuming ideal compositions ( $x = 0.15$ ;  $y = 0.10$ ). (b) Experimental data and calculations using the analyzed compositions.

100%  $\text{B}^4$ , which is not observed experimentally for these glasses. Instead, the NMR results indicate a competition between  $\text{B}^3$ -to- $\text{B}^4$  conversion and formation of NBOs on the  $\text{SiO}_4$  tetrahedra, with a preference for the former. The NMR data also show that NBOs can form on the  $\text{B}^3$  groups, but most of the NBOs are associated with  $\text{SiO}_4$  tetrahedra. In the high- $\text{B}_2\text{O}_3$  glasses, the  $\text{B}^3$ -to- $\text{B}^4$  conversion is much more favorable compared to NBO-on- $\text{SiO}_4$  formation; i.e., the counting rules of both the IC and Yun–Bray models are satisfied. The increasing discrepancy in the higher- $\text{SiO}_2$  regime indicates that the free energy associated with NBO formation on  $\text{SiO}_4$  takes an intermediate value compared to the  $\text{B}^3$ -to- $\text{B}^4$  conversion and NBO-on- $\text{B}^3$  formation.<sup>83</sup> This value appears close to the energy associated with  $\text{B}^3$ -to- $\text{B}^4$  conversion; i.e., there are competing enthalpic and entropic effects at play, in which the NBO formation on  $\text{SiO}_4$  becomes entropically favored when more  $\text{SiO}_4$  units are available.

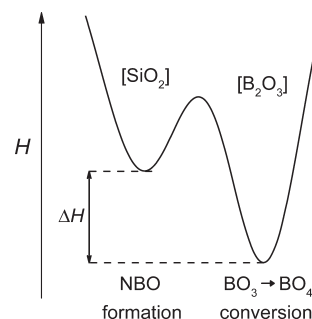


**Figure 7.** Schematic illustration of the two-state statistical mechanical model for boron speciation in borosilicate glasses. The model accounts for the enthalpy difference ( $\Delta H$ ) between NBO formation on Si and conversion of  $\text{B}^3$  to  $\text{B}^4$  upon addition of network modifying oxides to a borosilicate glass.

These effects can be described using a simple two-state statistical mechanical model. Here we consider the structure of the glass as being frozen in at a fictive temperature ( $T_f$ ), which depends on the thermal history of the glass.<sup>84</sup> Please note that the fictive temperature  $T_f$  has a different definition compared to the configurational temperature  $T_{\text{conf}}$  introduced previously. This difference is discussed in detail by Araujo and Mauro.<sup>81</sup> However, for a normally cooled glass (i.e., 10 K/s cooling rate), the fictive temperature can also be taken as equal to the glass transition temperature, i.e.,  $T_f = T_g$ .<sup>67</sup> The two-state model is schematically illustrated in Figure 7 and results in the following equation for the number of  $\text{B}^4$  units

$$c(\text{B}^4) = \min \left[ \frac{2(x+y)z}{z + (1-x-y-z) \exp[-\Delta H/kT_f]} z + \frac{2}{3}(1-x-y-z), 2z \right] \quad (13)$$

Here,  $k$  is Boltzmann's constant and  $\Delta H$  is the enthalpy difference between NBO formation and  $\text{B}^3$ -to- $\text{B}^4$  conversion. The first term in the minimum function of eq 13 applies when the  $\text{B}^4$  fraction is limited by the modifier concentration, whereas the second and third terms apply when there is excess modifier. According to the two-state model, the modifiers can be used for either  $\text{B}^3$ -to- $\text{B}^4$  conversion or NBO-on- $\text{SiO}_4$  formation when there is limited modifier concentration. The role of the modifiers is determined by the enthalpy difference between the two states (the enthalpic effect governed by  $\Delta H$ ) and the number of available boron vs silicon sites (the entropic effect governed by  $T_f$  and  $[\text{SiO}_2]$  vs  $[\text{B}_2\text{O}_3]$ ). For large enthalpy differences, the modifiers are more likely to be used for charge-balancing  $\text{B}^4$  units such that  $N_4$  would attain a large value. At higher fictive temperatures, the entropic effect plays a more dominant role and the modifiers are more randomly distributed among the two states, even though the  $\text{B}^3$ -to- $\text{B}^4$  conversion is enthalpically favored; i.e.,  $N_4$  attains a lower value. Likewise, for high  $\text{SiO}_2$  concentrations, owing to the entropy effect it becomes more difficult for the modifiers "to find" the boron sites, which also results in a lower value of  $N_4$ .

The third term in eq 13 imposes a maximum that all B atoms are eligible to become four-coordinated. However, if



we extend the random pair model of Gupta<sup>61</sup> to borosilicate compositions, this maximum evolves from  $z$  in the pure borate to  $2z$  in the high-SiO<sub>2</sub> borosilicates. Since there are six bonds for each four-coordinated boron pair B<sup>4</sup>–O–B<sup>4</sup> ( $z_4$ ) balanced with six bonds for each three-coordinated boron pair B<sup>3</sup>–O–B<sup>3</sup> ( $z_3$ ) and four bonds for each four-coordinated silicon

$$6z_4 = 6z_3 + 4c(\text{Si}^4) \quad (14)$$

$c(\text{B}^4)$  is equal to  $2z_4$ ; viz., eq 14 reduces to the second term in eq 13. Hence,  $N_4$  can be calculated as

$$N_4 = \left( \min \left[ \frac{2(x+y)z}{z + (1-x-y-z) \exp[-\Delta H/kT_f]}, z + \frac{2}{3}(1-x-y-z), 2z \right] \right) / 2z \quad (15)$$

Using the experimentally determined  $T_g$  values, Figure 6b reveals excellent agreement between this new two-state model and the NMR results taking  $\Delta H = 0.072$  eV as the sole fitting parameter. Hence, this model will be used in the following section when calculating the macroscopic glass properties. We note that our statistical mechanical model differs from those proposed in the 1980s by Araujo<sup>83,85,86</sup> and Bray et al.<sup>87</sup> in that our model does not associate separate energies with each of the structural units and therefore only contains a single fitting parameter. Finally, it should be mentioned that our current model of boron speciation (eq 15) does not apply to the high-modifier regime, since none of the glasses under study belong to this regime. However, such extension would be possible following the random pair model.<sup>34</sup>

### III. NETWORK TOPOLOGY AND PROPERTY PREDICTION

**A. Counting of Network-Forming Species.** Following our recent work on the soda lime borate system,<sup>35</sup> we consider the following types of network-forming species:

- Four-coordinated boron bonded to four bridging oxygens (B<sup>4</sup>).
- Three-coordinated boron (B<sup>3</sup>).
- Four-coordinated silicon (Si).
- Oxygen, including both bridging and nonbridging varieties (O).
- Network modifiers (Na and Ca) that create NBOs (M<sup>NB</sup>).

Here we consider two types of network-modifying cations: (i) those which convert boron from trigonal to tetrahedral coordination and (ii) those which create NBOs. These two types are considered separately in our model, even though each network-modifying cation in the real structure obviously can be partly associated with both B<sup>4</sup> and NBOs as a consequence of their high coordination number. In the first case, the effects of both the sodium and calcium on the network topology are accounted for with the additional linear and angular constraints on the boron. However, it should be noted that the modifier ion itself is not a part of the network and just serves in a charge-compensating role for the tetrahedral boron. In the second case, the modifiers are a part of the glass network, and hence each contributes three degrees of freedom to the network and associated linear constraints. As described in section III.B, these linear constraints are counted with the NBOs. Finally, it should also be noted that we treat NBOs as a whole and do not distinguish between

different types of NBOs in the topological model, even though the NMR data (section II.B) show that NBOs form on both B<sup>3</sup> and SiO<sub>4</sub> groups.

The total number of atoms in the system (eq 11) is equal to  $3 + 2z$ . Since the number of modifiers used for boron charge compensation equals the number of B<sup>4</sup> units, the total number of network-forming species ( $\Omega$ ) is given by

$$\Omega = 3 + 2z - \min \left[ \frac{2(x+y)z}{z + (1-x-y-z) \exp[-\Delta H/kT_f]}, z + \frac{2}{3}(1-x-y-z), 2z \right] \quad (16)$$

The fraction  $N$  of each network-forming species can then be calculated as follows:

$$N(\text{O}) = \frac{2 - (x+y) + z}{\Omega} \quad (17)$$

$$N(\text{Si}) = \frac{1 - x - y - z}{\Omega} \quad (18)$$

$$N(\text{B}^4) = \left( \min \left[ \frac{2(x+y)z}{z + (1-x-y-z) \exp[-\Delta H/kT_f]}, z + \frac{2}{3}(1-x-y-z), 2z \right] \right) / \Omega \quad (19)$$

$$N(\text{B}^3) = \left( 2z - \min \left[ \frac{2(x+y)z}{z + (1-x-y-z) \exp[-\Delta H/kT_f]}, z + \frac{2}{3}(1-x-y-z), 2z \right] \right) / \Omega \quad (20)$$

$$N(\text{M}^{\text{NB}}) = \left( 2(x+y) - \min \left[ \frac{2(x+y)z}{z + (1-x-y-z) \exp[-\Delta H/kT_f]}, z + \frac{2}{3}(1-x-y-z), 2z \right] \right) / \Omega \quad (21)$$

To calculate these fractions, we need to know the value of  $T_f$ , which for a standard cooling rate (i.e.,  $T_f = T_g$ ) will, in turn, be calculated from the temperature-dependent constraint model in section III.C. In other words, we obtain a transcendental equation for the glass transition temperature  $T_g$  that can be solved using an iterative approach. Details of this calculation will be described later in section III.C. Using these calculated values of  $T_g$ , Figure 8 plots the composition dependence of the molar fractions of each network-forming species as a function of the  $[\text{SiO}_2]/([\text{SiO}_2] + [\text{B}_2\text{O}_3])$  ratio, in which we have set  $x = [\text{Na}_2\text{O}] = 0.15$  and  $y = [\text{CaO}] = 0.10$ .

**B. Temperature-Dependent Constraint Model.** The number of constraints associated with a network-forming species depends on its coordination number ( $r$ ). In the following, we apply the  $(r/2)$  and  $(2r - 3)$  rules<sup>38</sup> to count the two-body radial and three-body angular constraints, respectively. Based on our previous studies<sup>34,35</sup> and knowledge about the glass network structure of borosilicates, we consider the following types of bond constraints:

- $\alpha$ : Si–O, B–O, and M<sup>NB</sup>–O linear constraints. There are two  $\alpha$  constraints at each oxygen, for both bridging and nonbridging varieties.



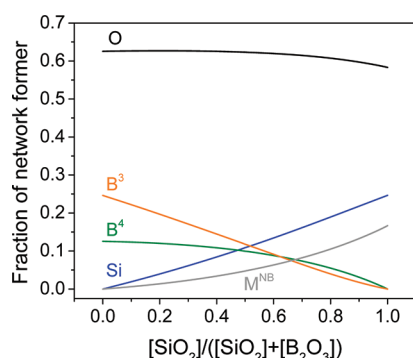


**Figure 8.** Fraction of the network-forming species in the ideal borosilicate system ( $x = 0.15$ ;  $y = 0.10$ ), following the analysis in section III.A using the two-state model for boron speciation.

- $\beta_{\text{Si}}$ : O–Si–O angular constraints. There are five  $\beta_{\text{Si}}$  constraints per Si to form a rigid Si tetrahedron.
- $\beta_{\text{B}}$ : O–B–O angular constraints. There are five  $\beta_{\text{B}}$  constraints per  $\text{B}^4$  and three  $\beta_{\text{B}}$  constraints per  $\text{B}^3$ .
- $\gamma$ : Si–O–Si, Si–O–B, B–O–B, Si–O– $\text{M}^{\text{NB}}$ , and B–O– $\text{M}^{\text{NB}}$  angular constraints. There is one  $\gamma$  constraint at each oxygen.
- $\mu$ : additional modifier rigidity due to clustering effects. Based on our previous findings for soda lime borate glasses,<sup>35</sup> we assign two  $\mu$  constraints per NBO-forming Na atom, but zero  $\mu$  constraints for Ca.

Please note that with this approach there is no need to consider the various types of superstructural units (e.g., boroxol rings), since these do not introduce any new *independent* constraints to the system. Furthermore, the constraint counting is performed only over the nearest neighbors; i.e., constraints from medium- and long-range interactions have been approximated from the two- and three-body constraints.

After identification and counting of the constraints, the next step is to order the constraints in terms of their relative bond strength, i.e., their constraint onset temperatures. Since the linear bonds are the strongest, the  $\alpha$  constraints freeze in at the highest temperature. The  $\mu$  constraint is also a two-body constraint, and therefore it is considered to be the second strongest. We also know that the angular constraints around Si ( $\beta_{\text{Si}}$ ) and B ( $\beta_{\text{B}}$ ) are stronger than those around O ( $\gamma$ ).<sup>88</sup> Due to the  $\text{sp}^3$  hybridization of Si, where four  $\text{sp}^3$ -hybridized Si orbitals are overlapped by oxygen's two bonding  $\text{sp}^3$  orbitals, the  $\beta_{\text{Si}}$  constraints are stronger than the  $\beta_{\text{B}}$  constraints. We can estimate the onset temperature of the  $\beta_{\text{B}}$  constraint ( $T_{\beta,\text{B}}$ ) from the  $T_{\beta}$  values of pure sodium borate ( $T_{\beta}^{\text{Na}} = 740 \text{ K}$ )<sup>34</sup> and calcium borate ( $T_{\beta}^{\text{Ca}} = 910 \text{ K}$ )<sup>89</sup> glasses and by assuming that  $T_{\beta,\text{B}}$  depends on the  $[\text{Na}_2\text{O}]/[\text{CaO}]$  ratio:<sup>35</sup>

$$T_{\beta,\text{B}}(x,y) = \left(\frac{2x}{2x+y}\right)T_{\beta}^{\text{Na}} + \left(\frac{y}{2x+y}\right)T_{\beta}^{\text{Ca}} \quad (22)$$

In summary, this gives the following ordering of constraint onset temperatures:

$$T_{\gamma} < T_{\beta,\text{B}} < T_{\beta,\text{Si}} < T_{\mu} < T_{\alpha} \quad (23)$$

In the region  $T_{\gamma} < T_{\text{g}}(x,y,z) < T_{\beta,\text{B}}(x,y)$ , the number of constraints per atom ( $n$ ) can then be calculated from the above analysis:

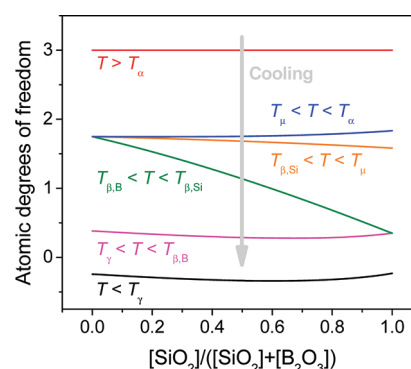


**Figure 9.** Composition and temperature dependence of the average number of atomic degrees of freedom in the ideal borosilicate system ( $x = 0.15$ ;  $y = 0.10$ ). The following types of constraints have been considered, in order of decreasing strength: ( $\alpha$ ) Si–O, B–O, and  $\text{M}^{\text{NB}}$ –O linear constraints; ( $\mu$ ) modifier rigidity due to clustering around NBO-forming sodium; ( $\beta_{\text{Si}}$ ) O–Si–O angular constraints; ( $\beta_{\text{B}}$ ) O–B–O angular constraints; and ( $\gamma$ ) Si–O–Si, Si–O–B, B–O–B, Si–O– $\text{M}^{\text{NB}}$ , and B–O– $\text{M}^{\text{NB}}$  angular constraints.

$$n(x,y,z) = 2N(\text{O}) + 5N(\text{Si}) + 5N(\text{B}^4) + 3N(\text{B}^3) + 2\left(\frac{2x}{2x+y}\right)N(\text{M}^{\text{NB}}) \quad (24)$$

Here, we have assigned all of the  $\alpha$  constraints on the oxygen and none on the cations. The corresponding number of atomic degrees of freedom is

$$f(x,y,z) = 3 - 2N(\text{O}) - 5N(\text{Si}) - 5N(\text{B}^4) - 3N(\text{B}^3) - 2\left(\frac{2x}{2x+y}\right)N(\text{M}^{\text{NB}}) \quad (25)$$

For  $T_{\beta,\text{B}}(x,y) < T_{\text{g}}(x,y,z) < T_{\beta,\text{Si}}$  the atomic degrees of freedom increase to

$$f(x,y,z) = 3 - 2N(\text{O}) - 5N(\text{Si}) - 2\left(\frac{2x}{2x+y}\right)N(\text{M}^{\text{NB}}) \quad (26)$$

In Figure 9, we have plotted the composition and temperature dependence of  $f$  for the  $x\text{Na}_2\text{O}-y\text{CaO}-z\text{B}_2\text{O}_3-(1-x-y-z)\text{SiO}_2$  system using the fractions of network-formers from Figure 8.

**C. Glass Transition Temperature.** Gupta and Mauro<sup>33,34</sup> have derived an expression for calculating  $T_{\text{g}}(x,y,z)$  relative to that of a reference composition  $(x,y,z)_{\text{R}}$

$$\frac{T_{\text{g}}(x,y,z)}{T_{\text{g}}((x,y,z)_{\text{R}})} = \frac{f(T_{\text{g}}((x,y,z)_{\text{R}}))}{f(T_{\text{g}}(x,y,z))} \quad (27)$$

Hence, by combining eqs 26 and 27,  $T_{\text{g}}(x,y,z)$  can be computed as

$$T_{\text{g}}(x,y,z) = \max\left[T_{\beta,\text{B}}(x,y), \frac{f(0.15,0.1,0)}{f(x,y,z)}T_{\text{g}}(0.15,0.1,0)\right] \quad (28)$$

where we have taken the  $\text{SiO}_2$  end-member glass as the reference composition. The glass transition temperature of the  $\text{SiO}_2$  end-member is obtained experimentally as 814 K (cf. Table 1). The

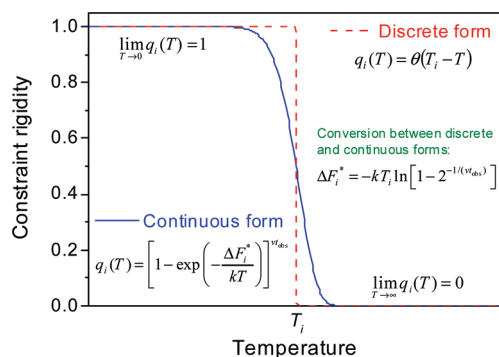


**Figure 10.** Temperature dependence of the rigidity ( $q$ ) of the bond constraint  $i$  with the onset temperature  $T_i$ .  $q_i(T)$  can be written in either continuous or discrete forms.<sup>33</sup> We use the discrete form for deriving an analytical formula for calculating  $T_g(x, y, z)$ , whereas the continuous form is required for numerically calculating  $m(x, y, z)$ . In the limits of low and high temperature the two forms converge, since all constraints are rigid and broken, respectively.

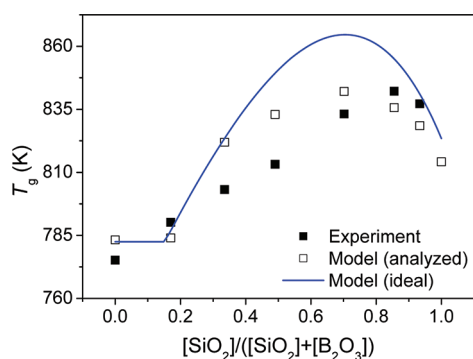


**Figure 11.** Composition dependence of the glass transition temperature for the borosilicate glasses. The filled points represent the experimental data points obtained from DSC measurements. The open points and the solid line represent the computed  $T_g(x, y, z)$  values with eq 28 using the analyzed and ideal ( $x = 0.15$ ;  $y = 0.10$ ) compositions, respectively.

maximum function in eq 28 is required, since eq 26 is not valid when  $T_g(x, y, z) < T_{\beta,B}(x, y)$  due to the assumption of floppy  $\beta_B$  constraints. This phenomenon is discussed in detail by Mauro et al.<sup>34</sup>

Next, we need to account for the temperature dependence of the constraints. This is quantified by  $q_i(T)$ , a measure of the rigidity for constraint  $i$  as a function of temperature. Both continuous and discrete (unit step approximation) forms of  $q_i(T)$  have been applied to calculate the composition dependence of  $T_g$ .<sup>34</sup> Using the discrete model, a bond constraint becomes suddenly floppy as the temperature is increased above the onset temperature of that constraint. In the continuous model, the bond constraint softens gradually over a range of temperatures. Mauro et al.<sup>34</sup> found little difference between  $T_g$  values calculated using the discrete and continuous forms of  $q_i(T)$ . Therefore, we apply the discrete form of  $q_i(T)$ , since this enables a simplified calculation of  $T_g(x, y, z)$ . A schematic illustration of the difference between the discrete and continuous forms of  $q_i(T)$  is presented in Figure 10. The two forms converge in the limits of both low and high temperature where all constraints are rigid and broken, respectively.

As mentioned in section III.A, we need to solve a transcendental equation in order to calculate  $T_g(x, y, z)$ , since knowledge of boron speciation is required for calculating  $T_g(x, y, z)$ , which in turn depends on  $T_g(x, y, z)$ . We calculate  $T_g(x, y, z)$  by using an initial guess value of  $T_g$  for all glasses and iterate until the  $T_g$  value converges. Figure 11 shows the experimental and computed values of  $T_g(x, y, z)$ . The agreement between predicted and measured values is remarkable, considering that only one fitting parameter is involved in the entire calculation, viz., the  $\Delta H$  parameter in the two-state model for boron speciation. Note that the glass transition temperature of a borate glass can be predicted from that of a silicate glass with only the topological degrees of freedom as the scaling parameter.

**D. Liquid Fragility Index.** According to the temperature-dependent constraint theory,<sup>33,34</sup> the liquid fragility index can be computed as

$$m(x, y, z) = m_0 \left( 1 + \frac{\partial \ln f(T, x, y, z)}{\partial \ln T} \right)_{T=T_g(x, y, z)} \quad (29)$$

Since this calculation of  $m(x, y, z)$  involves taking the temperature derivative of  $f(T, x, y, z)$ , we must apply a continuous form of  $q_i(T)$ . According to an energy landscape analysis<sup>76</sup> and recent molecular dynamics simulations,<sup>50</sup>  $q_i(T)$  can be calculated as a continuous function of temperature

$$q_i(T) = \left[ 1 - \exp \left( - \frac{\Delta F_i^*}{kT} \right) \right]^{v_{\text{obs}}} \quad (30)$$

where  $\Delta F_i^*$  is the activation energy for breaking the  $i$  constraint,  $v$  the vibrational attempt frequency, and  $t_{\text{obs}}$  the observation time. As illustrated in Figure 10,  $\Delta F_i^*$  is correlated with the constraint onset temperature  $T_i$ :

$$\Delta F_i^* = -kT_i \ln[1 - 2^{-1/(v_{\text{obs}})}] \quad (31)$$

For our previous topological model for the soda lime borate glass system, we employed  $v_{\text{obs}}$  as the sole fitting parameter and found it to be equal to 60.<sup>35</sup> We will use this value for our calculations of  $m(x, y, z)$ .

The computation of  $m(x, y, z)$  requires association of onset temperatures with each constraint. We calculate  $T_{\beta,B}$  using eq 22, and we know that  $T_\gamma$  is equal to 328 K for B–O–B constraints.<sup>34</sup> As an approximation, we assume that the  $\gamma$  bond-bending constraints around oxygen have the same strength independent of the neighboring atoms. The  $\alpha$  constraints freeze in at the highest temperature due to their two-body nature. We set  $T_\alpha$  equal to 1600 K, since it must be above the glass transition temperature of pure  $\text{SiO}_2$  glass ( $\sim 1473$  K) and the  $m(x, y, z)$  results turn out to be relatively insensitive to the actual value of  $T_\alpha$  (e.g.,  $m$  changes by less than 2% if we set  $T_\alpha$  to 2000 K). We treat  $T_\mu$  as a fitting parameter that must be somewhat less than  $T_\omega$  since this constraint is also two-body in nature but expected to be weaker than the  $\alpha$  constraints. We also treat  $T_{\beta,\text{Si}}$  as a fitting parameter in our calculation and require  $T_{\beta,\text{Si}} \leq T_{\omega}$  since the  $\beta_{\text{Si}}$  constraint is three-body in nature. We obtain  $T_{\beta,\text{Si}} = T_\mu = 1425$  K. Figure 12a shows that the agreement between experimental and computed values of  $m(x, y, z)$  is excellent. Other values of  $T_\omega$ ,  $T_{\beta,\text{Si}}$ , and  $T_\mu$  could have given similar curves, since the calculations are fairly insensitive to the specific values of these onset temperatures. Hence, we have captured the shape of the experimental  $m(x, y, z)$  curve since we have accurately accounted for

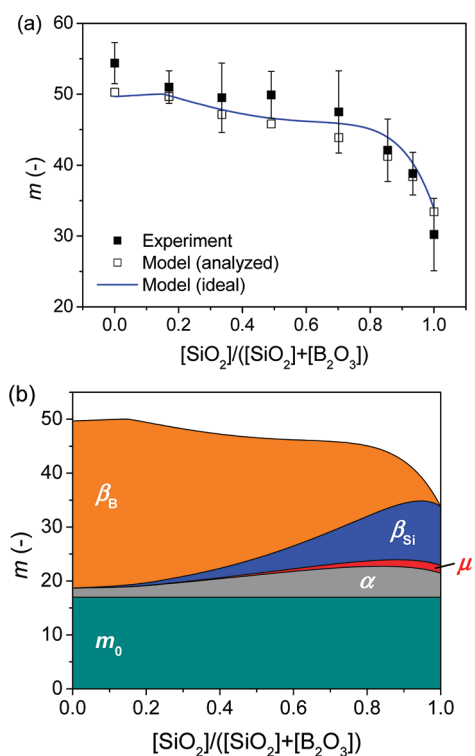


**Figure 12.** (a) Composition dependence of the liquid fragility index ( $m$ ) for the borosilicate glasses. The filled points represent the experimental data points obtained from DSC measurements. The open points and the solid line represent the computed  $m(x, y, z)$  values with eq 29 using the analyzed and ideal ( $x = 0.15$ ;  $y = 0.10$ ) compositions, respectively. (b) Composition dependence of the computed  $m(x, y, z)$  values showing the contributions from the different constraints. The  $\gamma$  constraints have a negligible impact on  $m(x, y, z)$  and can therefore not be seen in the plot.

the number of constraints associated with each network-forming species. This also allows us to perform model calculations of  $\Delta C_p(x, y, z)$  using eq 10, since we now have accurate models for both  $T_g(x, y, z)$  and  $m(x, y, z)$ . The composition dependence of  $\Delta C_p$  with  $A = 19$  kJ/mol is illustrated in Figure 13.

There has been intensive research in understanding the microstructural and topological origin of liquid fragility,<sup>90–94</sup> yet key questions remain unanswered. To understand the microscopic mechanisms behind the composition dependence of fragility in borosilicates, we have illustrated the influence of the various constraints on  $m(x, y, z)$  in Figure 12b. This plot reveals that the  $\gamma$  and  $\mu$  constraints have a negligible impact on  $m(x, y, z)$ . In contrast, we find that the O–B–O angular constraints are the main contributors in making the soda lime borosilicates “fragile”; i.e., the scaling of fragility with composition is primarily a consequence of the changing concentration of O–B–O angles. This finding agrees with our previous result for the soda lime borate system.<sup>35</sup>

**E. Glass Hardness. Experimental Procedure.** The Vickers hardness ( $H_V$ ) of a glass is defined as the ratio of the indentation load to the indentation surface area and correlates with the material's resistance to permanent deformation. We determined  $H_V$  of the polished glass samples by using a Duramin 5 (Struers) microindenter. The indentations were performed at a load of 0.25 N for durations of 5 s. The hardness of each sample was measured at 30 widely separated locations.

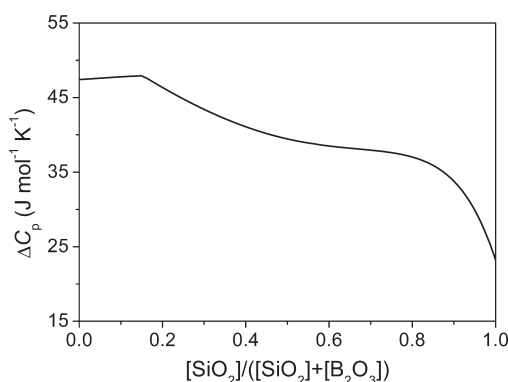


**Figure 13.** Model calculation of the composition dependence of the change in the isobaric heat capacity during the glass transition. The change is quantified by  $\Delta C_p(x, y, z) = C_{p,l} - C_{p,g}$  where  $C_{p,l}$  and  $C_{p,g}$  are the liquid and glass heat capacity, respectively.  $\Delta C_p(x, y, z)$  has been calculated using eq 10 with  $A = 19$  kJ/mol and the modeled values of  $T_g(x, y, z)$  (Figure 11) and  $m(x, y, z)$  (Figure 12a) for ideal compositions ( $x = 0.15$ ;  $y = 0.10$ ).

**Results and Modeling.** Figure 14a illustrates the composition dependence of the experimentally determined  $H_V$  values. The samples become harder as more constraints associated with  $\text{SiO}_2$  are introduced into the glass network, up to a  $\text{SiO}_2$  concentration of around 62 mol %, and then the hardness decreases with further addition of  $\text{SiO}_2$ . For alkali–alkaline earth–borate glasses, we have recently demonstrated that the composition dependence of  $H_V$  can be quantitatively predicted using temperature-dependent constraint theory.<sup>9</sup> In detail, we found that the glass network must be rigid in at least two dimensions to have a nonzero hardness; i.e., a critical number of 2.5 constraints per atom ( $n_{\text{crit}} = 2.5$ ) must be present. A fully three-dimensional isostatic network ( $n = 3$ ) has more than enough constraints to provide resistance to the incoming indenter. Rigidity along one dimension ( $n = 2$ , as in selenium) corresponds to a chain structure that cannot provide sufficient resistance against the applied stress during indentation. A rigid two-dimensional layer structure ( $n = 2.5$ , as in graphene) also does not provide enough constraints to provide resistance, but additional layer-locking constraints in the third dimension (i.e., constraints in excess of  $n = 2.5$ ) results in nonzero hardness.<sup>9</sup>

Hardness is thus governed by the number of constraints in excess of 2.5, with only an unknown proportionality constant ( $dH_V/dn$ ):

$$H_V(x, y, z) = \left( \frac{dH_V}{dn} \right) [n(x, y, z) - 2.5] \quad (32)$$

Here, the number of constraints  $n(x, y, z)$  must be calculated at the temperature at which the hardness measurements are conducted (in this case, room temperature). In this section, we investigate whether eq 32 can also be used to predict the hardness of borosilicate glasses, i.e., whether  $n_{\text{crit}} = 2.5$  is a universal value for all oxide glasses and if  $dH_V/dn$  depends on composition. To do so, we calculate  $n(x, y, z)$  for  $T < T_g$ , where all bond bending constraints are intact:

$$n(x, y, z) = 3N(\text{O}) + 5N(\text{Si}) + 5N(\text{B}^4) + 3N(\text{B}^3) + 2 \left( \frac{2x}{2x + y} \right) N(\text{M}^{\text{NB}}) \quad (33)$$



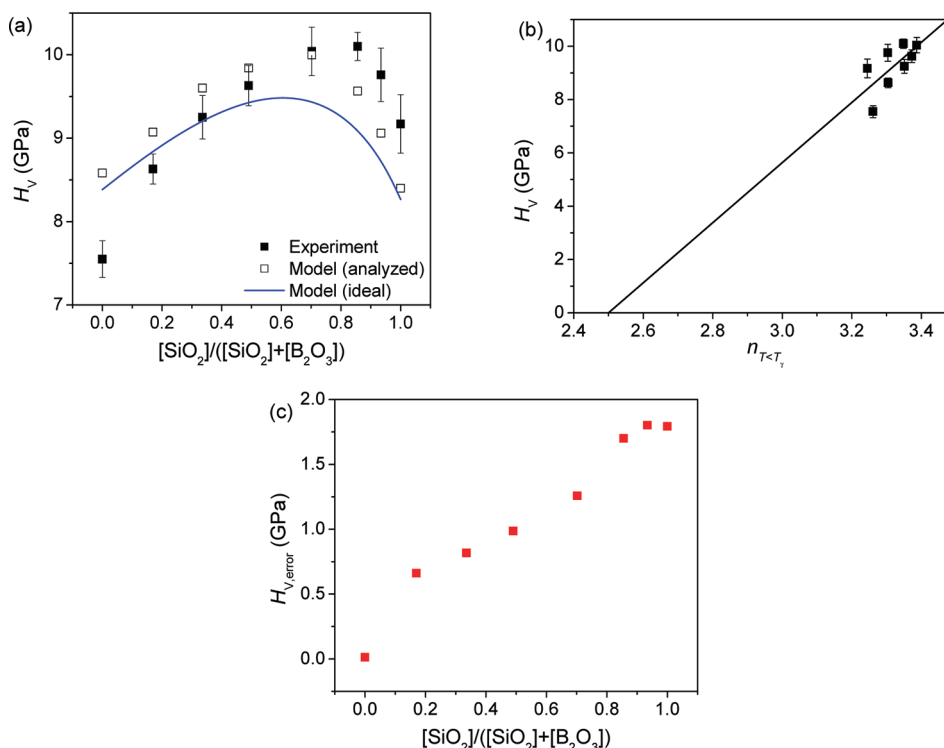


**Figure 14.** (a) Composition dependence of Vickers hardness ( $H_V$ ) for the borosilicate glasses. The filled points represent the experimental data points, whereas the open points and the solid line represent the computed  $H_V(x, y, z)$  values with eq 32 ( $dH_V/dn = 11.3$  GPa) using the analyzed and ideal ( $x = 0.15$ ;  $y = 0.10$ ) compositions, respectively. (b) Measured Vickers hardness as a function of the average number of room temperature constraints ( $T < T_g$ ) constraints (eq 33). The solid line represents eq 32 with  $dH_V/dn = 11.3$  GPa. (c) Absolute error in predicting Vickers hardness ( $H_{V,error}$ ) when using  $dH_V/dn = 9.9$  GPa.<sup>9</sup>

With this expression for  $n(x, y, z)$  inserted into eq 32, we find that hardness also scales linearly with the number of room temperature constraints for borosilicate glasses (Figure 14b). Even though the glasses vary from pure borate to pure silicate end members,  $n_{crit} = 2.5$  appears to be a universal value for all glassy networks.  $dH_V/dn$  is found experimentally to be equal to 11.3 GPa. Using this value, we find good agreement between the predicted and measured values of hardness (Figure 14a).

Figure 14c shows the error in predicting Vickers hardness ( $H_{V,error}$ ) when using the proportionality constant  $dH_V/dn = 9.9$  GPa for the soda lime borate glasses determined in ref 9.  $H_{V,error}$  is found to increase with increasing silica content. This could have two possible origins. First, the proportionality constant  $dH_V/dn$  could be composition dependent, which could be explained as follows. There are mainly two modes by which a glass deforms under a sharp contact loading, i.e., plastic or shear flow (volume conservation) and densification (volume contraction).<sup>95,96</sup> It is possible that two glasses have the same value of  $H_V$  even though they can have different contributions of shear flow and densification to the indentation deformation. The indentation deformation for glasses exhibiting low atomic packing density or Poisson's ratio (such as silica) is governed by densification, whereas that for glasses with high atomic packing density or Poisson's ratio (such as soda lime silicate) is governed by shear plasticity.<sup>96,97</sup> For sodium borate glasses, Yoshida et al.<sup>98</sup> found that the deformation mechanism had a large contribution of densification for various  $[\text{Na}_2\text{O}]/[\text{B}_2\text{O}_3]$  ratios due to the relatively easy rearrangement of B–O ring

structures. Hence, the addition of three-coordinated boron species into a silica glass makes the network less rigid, which allows densification under stress.<sup>99</sup> Therefore, the change in deformation mechanism with varying  $[\text{SiO}_2]/[\text{B}_2\text{O}_3]$  ratio could be the origin of the composition dependence of  $dH_V/dn$ .

Second, we may not have accurately accounted for all room temperature constraints in our model (section III.B). Unless these missing constraints are rigid only at low temperatures, they would also influence the calculation of  $T_g(x, y, z)$ . However, we did not find an increasing error in predicting  $T_g$  with increasing  $\text{SiO}_2$  content (Figure 11). For example, the missing constraints could be constraints from medium- or long-range interactions that are neglected in the current model. However, we find that most of the error associated with predicting  $H_V$  can be explained by assuming that there are two  $\mu$  constraints associated with each NBO-forming Ca atom in addition to the two  $\mu$  constraints per NBO-forming Na atom (Figure 15). This assumption provides a better linear fit of hardness vs the number of room temperature constraints (Figure 15a), with  $dH_V/dn = 10.4$  GPa. Figure 15b compares measured and computed values of  $H_V$  for different model assumptions. The error in predicting hardness clearly becomes smaller with the assumption of rigid Ca atoms and when using the new value of  $dH_V/dn$  equal to 10.4 GPa. For this explanation to be valid, the  $\mu$  constraints associated with Ca should have a much lower onset temperature than those associated with Na.

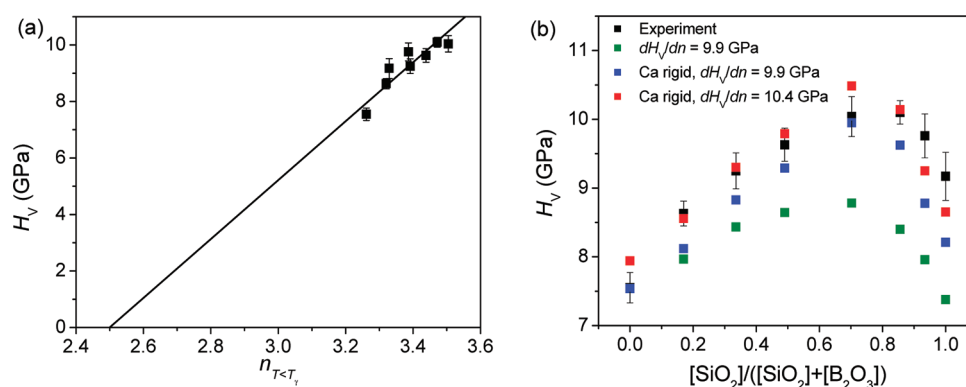


**Figure 15.** (a) Measured Vickers hardness ( $H_V$ ) as a function of the average number of room temperature ( $T < T_g$ ) constraints assuming two  $\mu$  constraints per NBO-forming Ca atom. The solid line represents eq 32 with  $dH_V/dn = 10.4$  GPa. (b) Composition dependence of Vickers hardness for experimental data (black squares) and model calculations using eq 32 with  $dH_V/dn = 9.9$  GPa (green squares),  $dH_V/dn = 9.9$  GPa and assuming rigid NBO-forming Ca atoms (blue squares), and  $dH_V/dn = 10.4$  GPa and assuming rigid NBO-forming Ca atoms (red squares).

## IV. DISCUSSION

**A. Quantitative Design of New Glasses.** We have demonstrated that temperature-dependent constraint theory is a powerful tool for predicting the composition dependence of macroscopic glass properties for complex oxide glasses. In this work, we have extended the approach to a mixed network former system. Our model can be applied to quantitatively design borosilicate glasses with desired properties without having to melt glasses across an entire phase space. For example, Figure 16 shows model calculations of  $T_g(x, y, z)$  for two different borosilicate systems. Figure 17 shows model calculations of  $N_4(x, y, z)$ ,  $T_g(x, y, z)$ , and  $H_V(x, y, z)$  for a sodium borosilicate system.

**B. Glass Transition Temperature of  $\text{SiO}_2$ .** For high silica contents, the glass transition temperature increases rapidly with increasing  $[\text{SiO}_2]/[\text{Na}_2\text{O}]$  ratio (Figure 16a). According to our model, the pure  $\text{SiO}_2$  glass is isostatic ( $f = 0$ ), which means that  $T_g$  goes to infinity for  $T_{\beta, \text{B}}(x, y) < T_g(x, y, z) < T_{\beta, \text{Si}}$  (eq 28). Of course, this dramatic change in  $T_g$  with composition is not in agreement with experimental data. This suggests that the  $\beta_{\text{Si}}$  constraints soften before the glass transition temperature is reached and/or that short-range defects lower the number of constraints. Such intrinsic defects could include  $\text{Si}-\text{O}-\text{O}-\text{Si}$  or  $\text{Si}-\text{O}-\text{O}-\text{Si}$  peroxy bridges and silicon atoms with three neighboring oxygens.<sup>100,101</sup> Our results therefore provide a natural explanation for the dramatic drop in the  $T_g$  of  $\text{SiO}_2$  with the addition of ppm levels of alkali oxide or water.<sup>102,103</sup> Namely, the slope of the change of  $T_g(x, y, z)$  with  $f(x, y, z)$  is very high for nearly isostatic  $\text{SiO}_2$  (eq 28); i.e., even the addition of ppm levels of impurities that increase  $f(x, y, z)$  will have a significant impact on the glass transition temperature.

**C. Temperature-Dependent Structural Units and Constraints.** In comparison with our previous work,<sup>34,35</sup> we have included temperature-dependent changes in the short-range structure of the system; viz., the temperature-dependence of boron atoms is accounted for by using a two-state statistical mechanical model for boron speciation (eq 13). In addition, the different scaling of  $T_g(x, y, z)$  and  $H_V(x, y, z)$  with composition in Figure 17 illustrates the importance of accounting for the temperature dependence of the constraints. We also note that there is no clear correlation between boron speciation and  $H_V$ , even though there are five rigid  $\beta_{\text{B}}$  constraints for every

tetrahedrally coordinated boron and only three rigid  $\beta_{\text{B}}$  constraints for every trigonally coordinated boron. This is because the introduction of  $\text{SiO}_2$  changes both the total number of constraints and boron speciation. In agreement with experimental observations,<sup>29</sup> we have not included temperature-dependent speciation of the silicate units. However, a possible improvement of the current model would be to account for the composition dependence of the parameter  $B$  of the Adam–Gibbs relation.<sup>53</sup> In the calculation of  $T_g(x, y, z)$ , it is assumed that  $B(x, y, z)$  is constant.<sup>33</sup> Although this assumption is valid for narrow composition ranges,<sup>104</sup> the system investigated in this work spans from pure borate to pure silicate end members.

Figure 18 shows how the number of constraints evolves with composition at room temperature. This figure is useful for clarifying the relative impact of each type of constraint on hardness. For example, we find that the number of  $\gamma$  constraints slightly decreases with increasing  $[\text{SiO}_2]/[\text{B}_2\text{O}_3]$  ratio due to the decrease of  $N(\text{O})$ . Figure 18 also reveals that the number of  $\beta_{\text{B}}$  constraints decreases faster than the number of  $\beta_{\text{Si}}$  constraints increases with increasing  $[\text{SiO}_2]/[\text{B}_2\text{O}_3]$  ratio and that the impact of the  $\mu$  constraints on the total number of constraints is essentially negligible for the low- $\text{B}_2\text{O}_3$  glasses. In comparison, Figure 12b shows how the number of constraints impacts fragility. While the  $\alpha$  and  $\gamma$  constraints contribute significantly to the total number of room temperature constraints controlling hardness, these constraints play only a minor role in governing liquid fragility. Hence, besides being a useful approach for calculating glass properties as a function of composition, topological constraint theory is also a powerful tool for understanding the underlying structural and topological origins of glass properties.

**D. Thermal History Dependence of Boron Speciation and Constraints.** Boron speciation in borosilicate glasses depends on composition,<sup>11–14</sup> temperature (thermal history),<sup>28–30</sup> and pressure.<sup>105–108</sup> Assuming isobaric conditions, we have accounted for both composition and temperature effects in the two-state model (eq 15). In our property predictions, we have assumed normally cooled glasses ( $T_f = T_g$ ), but glasses can be prepared with a wide range of thermal histories<sup>109</sup> and glasses relax toward the supercooled liquid state over time. Therefore, here we investigate the influence of fictive temperature on  $H_V$  by first calculating  $N_4$  using eq 15 as a function of fictive temperatures for a fixed composition.

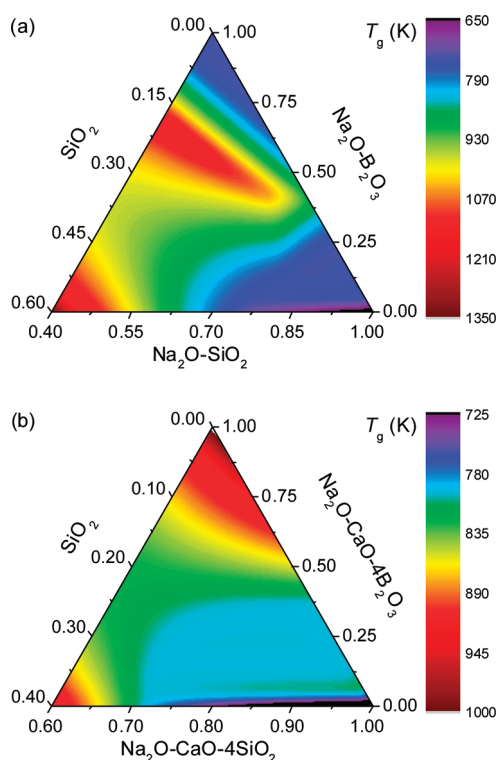


**Figure 16.** Model calculations of  $T_g(x, y, z)$  for (a) soda borosilicate and (b) soda lime borosilicate systems.  $T_g(x, y, z)$  is calculated using eq 28.

We then recalculate the number of constraints and use these to calculate  $H_V$  using eq 32 with  $dH_V/dn = 10.4$  GPa and the assumption of rigid Ca atoms.

We have performed such calculations for three ideal compositions ( $x = 0.15$ ;  $y = 0.10$ ), for which  $z = 0.375$  (Figure 19a),  $z = 0.15$  (Figure 19b), and  $z = 0.60$  (Figure 19c). For  $z = 0.375$ , the  $\text{SiO}_2$  and  $\text{B}_2\text{O}_3$  concentrations are identical, and we find that there is a pronounced (experimentally detectable) thermal history dependence of  $N_4$  and  $H_V$ . For the high- $\text{SiO}_2$  glass ( $z = 0.15$ ) this dependence becomes even more pronounced, whereas it nearly vanishes (i.e., around or below experimental detection limit) for the high- $\text{B}_2\text{O}_3$  glass. These calculations illustrate the importance of accounting for both composition and thermal history when attempting to predict glass properties.

To identify whether these model predictions of the thermal history dependence are reasonable, we consider the available literature data of the impact of  $T_f$  on  $N_4$ . For sodium borosilicate glasses,  $^{11}\text{B}$  MAS NMR data have confirmed that the change in  $N_4$  with  $T_f$  becomes larger with increasing  $[\text{SiO}_2]/[\text{B}_2\text{O}_3]$  ratio.<sup>29,110</sup> Furthermore, for pure sodium borate glasses, Stebbins and co-workers<sup>28,29</sup> did not observe a fictive temperature dependence of boron speciation in agreement with eq 15. Here, we have compared experimental observations<sup>28,29,110,111</sup> with our model predictions of the change in  $N_4$  with  $T_f$ . This is shown in Figure 20, in which we have plotted experimental and predicted values of  $N_4$  as a function of  $T_f$ . The model predictions using eq 15 have been carried out by individually adjusting the  $\Delta H$  parameter for the glass with the lowest  $T_f$  value. Using that value of  $\Delta H$  for each glass, we find reasonably good agreement between experiments and model predictions. Part of the reason for the discrepancies could be that the compositions of these glasses from literature<sup>28,29,110,111</sup> are given as nominal rather than analyzed compositions. In future work,

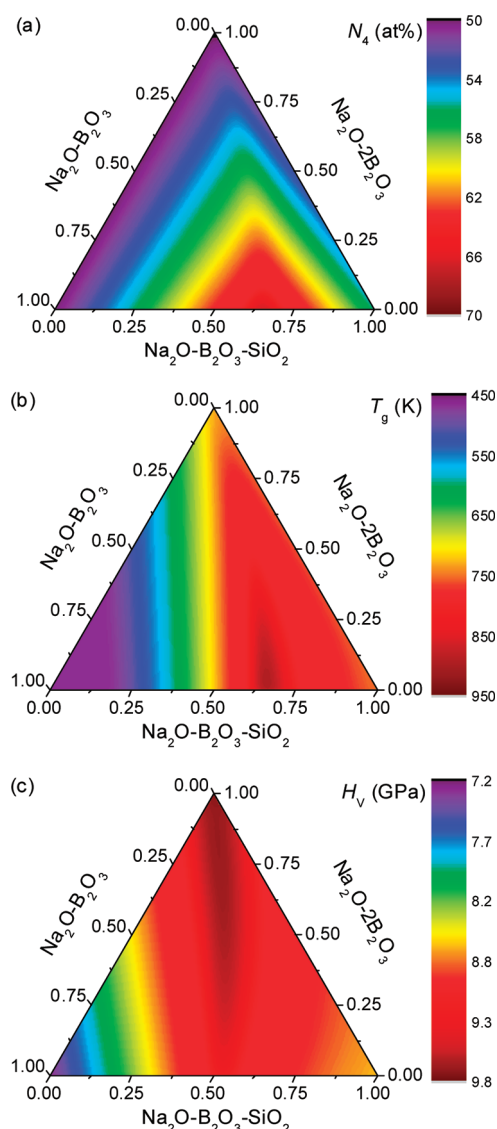


**Figure 17.** Model calculations of (a)  $N_4(x, y, z)$ , (b)  $T_g(x, y, z)$ , and (c)  $H_V(x, y, z)$  for a soda borosilicate system.  $N_4(x, y, z)$  is calculated using eq 15 with  $\Delta H = 0.072$  eV,  $T_g(x, y, z)$  is calculated using eq 28, and  $H_V(x, y, z)$  is calculated using eq 32 with  $dH_V/dn = 11.3$  GPa.

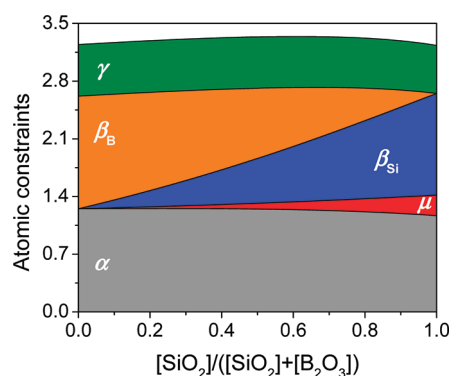


**Figure 18.** Composition dependence of the various types of atomic constraints calculated at room temperature (i.e., all constraints are rigid) and assuming ideal ( $x = 0.15$ ;  $y = 0.10$ ) compositions.



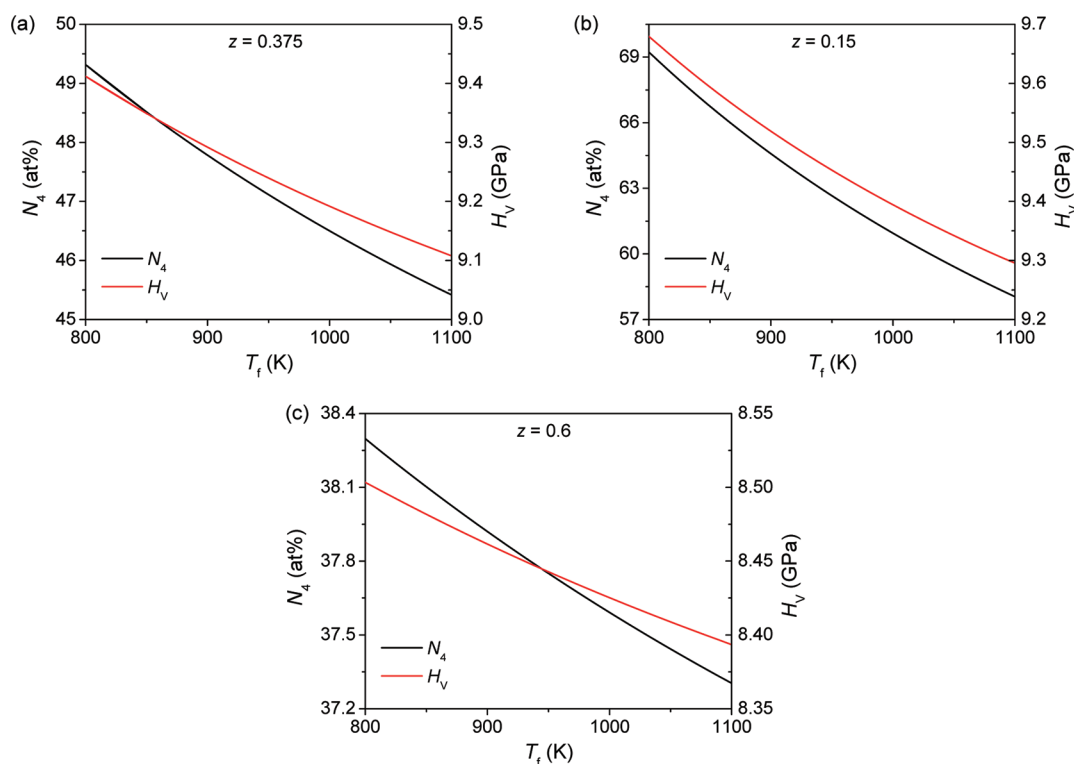


**Figure 19.** Model predictions of the thermal history (i.e., fictive temperature) dependence of boron speciation and Vickers hardness for ideal compositions ( $x = 0.15$ ;  $y = 0.10$ ) with  $z = 0.375$  (a),  $z = 0.15$  (b), and  $z = 0.60$  (c).  $N_4$  has been predicted using eq 15 with  $\Delta H = 0.072$  eV, whereas  $H_V$  has been calculated using eq 32 with  $dH_V/dn = 10.4$  GPa and assumption of rigid Ca atoms.

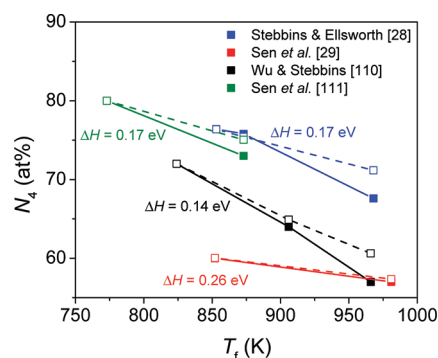


**Figure 20.** Influence of fictive temperature ( $T_f$ ) on fraction of tetrahedral to total boron ( $N_4$ ) in various borosilicate glasses from literature. The closed points and solid lines are the experimental data, whereas the open points and dashed lines are the model predictions using eq 15. The  $\Delta H$  parameter of the two-state speciation model was individually optimized to fit the lowest  $T_f$  value of each glass, and its value is shown next to the data points.

it would be interesting to also study the role of fictive pressure on glass properties; i.e., pressure-dependent constraint theory should be developed.

## V. CONCLUSIONS

A temperature-dependent constraint model of soda lime borosilicate glasses has been established offering quantitative prediction of the structure–topology–property relations in these glasses. Application of constraint theory requires knowledge of

the speciation of the network-forming structural units. We have therefore proposed a simple two-state statistical mechanical model of boron speciation considering the competition between NBO formation and coordination change of boron. This model accurately captures the change in boron coordination with only a single fitting parameter, viz., the enthalpy difference between  $B^3$ -to- $B^4$  conversion and the formation of NBOs on  $SiO_4$  tetrahedra. The model also accounts for the thermal history dependence of boron speciation through incorporation of a fictive temperature, which is equal to the glass transition temperature for a normally cooled glass. Building on this two-state model, a detailed topological analysis of the glass system has been performed by associating temperature-dependent constraints with each of the network-forming units. This model enables prediction of properties such as the glass transition temperature, liquid fragility, hardness, and the jump in heat capacity at the glass transition. Good agreement has been found between measured and predicted property values across the extremes from pure borate to pure silicate end members. This indicates that the temperature-dependent constraint theory can be universally applied in the prediction of macroscopic properties of network glasses. Moreover, the approach can be applied to understand the microstructural origins of glass properties. For example, the approach is used to describe how the various constraints affect fragility and the dramatic decrease in the  $T_g$  of pure silica glass upon modifier addition. The approach can also be applied to design glasses with optimized properties based on their composition and thermal history.

## AUTHOR INFORMATION

### Corresponding Author

\*Tel. +1 607-974-2185; e-mail mauroj@corning.com.

## ACKNOWLEDGMENT

The authors thank M. J. Dejneka of Corning Incorporated for stimulating discussions.

## REFERENCES

- (1) Varshneya, A. K. *Fundamentals of Inorganic Glasses*; Society of Glass Technology: Sheffield, U.K., 2006.
- (2) Kerner, R. *Models of Agglomeration and Glass Transition*; Imperial College Press: London, U.K., 2007.
- (3) Kurkjian, C. R.; Prindle, W. R. *J. Am. Ceram. Soc.* **1998**, *81*, 795–813.
- (4) Ellison, A.; Cornejo, I. A. *Int. J. Appl. Glass Sci.* **2010**, *1*, 87–103.
- (5) Wray, P. *Am. Ceram. Soc. Bull.* **2011**, *90* (4), 25.
- (6) Wright, A. C. *Phys. Chem. Glasses: Eur. J. Glass Sci. Technol. B* **2010**, *51*, 1–39.
- (7) Shelby, J. E. *J. Am. Ceram. Soc.* **1983**, *66*, 225–227.
- (8) Lower, N. P.; McRae, J. L.; Feller, H. A.; Betzen, A. R.; Kapoor, S.; Affatigato, M.; Feller, S. A. *J. Non-Cryst. Solids* **2001**, *293–295*, 669–675.
- (9) Smedskjaer, M. M.; Mauro, J. C.; Yue, Y. Z. *Phys. Rev. Lett.* **2010**, *105*, 115503.
- (10) Guan, M. J.; Wang, X.; Zhuang, Y. X.; Lin, G.; Xie, J. H.; Smedskjaer, M. M.; Qiu, J. R. *J. Electrochem. Soc.* **2011**, *158*, G151–G154.
- (11) Yun, Y. H.; Bray, P. J. *J. Non-Cryst. Solids* **1978**, *27*, 363–380.
- (12) Yun, Y. H.; Feller, S. A.; Bray, P. J. *J. Non-Cryst. Solids* **1979**, *33*, 273–277.
- (13) Dell, W. J.; Bray, P. J.; Xiao, S. Z. *J. Non-Cryst. Solids* **1983**, *58*, 1–16.
- (14) Wang, S. H.; Stebbins, J. F. *J. Non-Cryst. Solids* **1998**, *231*, 286–290.
- (15) Sen, S. *J. Non-Cryst. Solids* **1999**, *253*, 84–94.
- (16) Parkinson, B. G.; Holland, D.; Smith, M. E.; Howes, A. P.; Scales, C. R. *J. Phys.: Condens. Matter* **2007**, *19*, 415114.
- (17) Manara, D.; Grandjean, A.; Neuville, D. R. *J. Non-Cryst. Solids* **2009**, *355*, 2528–2531.
- (18) Angeli, F.; Charpentier, T.; de Ligny, D.; Cailleteau, C. *J. Am. Ceram. Soc.* **2010**, *93*, 2693–2704.
- (19) Du, L. S.; Stebbins, J. F. *Chem. Mater.* **2003**, *15*, 3913–3921.
- (20) Du, L. S.; Stebbins, J. F. *J. Phys. Chem. B* **2003**, *107*, 10063–10076.
- (21) Soules, T. F.; Varshneya, A. K. *J. Am. Ceram. Soc.* **1981**, *64*, 145–150.
- (22) Guo, F.; Greaves, G. N.; Smith, W.; Winter, R. *J. Non-Cryst. Solids* **2001**, *293–295*, 539–546.
- (23) Nanba, T.; Nishimura, M.; Miura, Y. *Geochim. Cosmochim. Acta* **2004**, *68*, 5103–5111.
- (24) Vedishcheva, N. M.; Shakhmatkin, B. A.; Wright, A. C. *Phys. Chem. Glasses* **2003**, *44*, 191–196.
- (25) Vedishcheva, N. M.; Shakhmatkin, B. A.; Wright, A. C. *J. Non-Cryst. Solids* **2004**, *345–346*, 39–44.
- (26) Silver, A. H.; Bray, P. J. *J. Chem. Phys.* **1958**, *29*, 984–990.
- (27) Silver, A. H.; Bray, P. J. *J. Chem. Phys.* **1960**, *32*, 288–292.
- (28) Stebbins, J. F.; Ellsworth, S. E. *J. Am. Ceram. Soc.* **1996**, *79*, 2247–2256.
- (29) Sen, S.; Xu, Z.; Stebbins, J. F. *J. Non-Cryst. Solids* **1998**, *226*, 29–40.
- (30) Kiczanski, T. J.; Du, L. S.; Stebbins, J. F. *J. Non-Cryst. Solids* **2005**, *351*, 3571–3578.
- (31) Wondraczek, L.; Mauro, J. C. *J. Eur. Ceram. Soc.* **2009**, *29*, 1227–1234.
- (32) Kieu, L.-H.; Delaye, J.-M.; Cormier, L.; Stolz, C. *J. Non-Cryst. Solids* **2011**, *357*, 3313–3321.
- (33) Gupta, P. K.; Mauro, J. C. *J. Chem. Phys.* **2009**, *130*, 094503.
- (34) Mauro, J. C.; Gupta, P. K.; Loucks, R. J. *J. Chem. Phys.* **2009**, *130*, 234503.
- (35) Smedskjaer, M. M.; Mauro, J. C.; Sen, S.; Yue, Y. Z. *Chem. Mater.* **2010**, *22*, 5358–5365.
- (36) Mauro, J. C. *Am. Ceram. Soc. Bull.* **2011**, *90* (4), 31.
- (37) Kerner, R.; Phillips, J. C. *Solid State Commun.* **2000**, *117*, 47–51.
- (38) Phillips, J. C. *J. Non-Cryst. Solids* **1979**, *34*, 153–181.
- (39) Phillips, J. C.; Thorpe, M. F. *Solid State. Commun.* **1985**, *53*, 699–702.
- (40) He, H.; Thorpe, M. F. *Phys. Rev. Lett.* **1985**, *54*, 2107–2110.
- (41) Senapati, U.; Varshneya, A. K. *J. Non-Cryst. Solids* **1995**, *185*, 289–296.
- (42) Thorpe, M. F. *J. Non-Cryst. Solids* **1995**, *182*, 135–142.
- (43) Georgiev, D. G.; Boolchand, P.; Micoulaut, M. *Phys. Rev. B* **2000**, *62*, R9228.
- (44) Micoulaut, M.; Phillips, J. C. *Phys. Rev. B* **2003**, *67*, 104204.
- (45) Mauro, J. C.; Varshneya, A. K. *J. Am. Ceram. Soc.* **2007**, *90*, 192–198.
- (46) Naumis, G. G. *Phys. Rev. E* **2005**, *71*, 026114.
- (47) Gjersing, E. L.; Sen, S.; Youngman, R. E. *Phys. Rev. B* **2010**, *82*, 014203.
- (48) Yang, G.; Bureau, B.; Rouxel, T.; Gueguen, Y.; Gulbitten, O.; Roiland, C.; Soignard, E.; Yarger, J. L.; Sangleboeuf, J.-C.; Lucas, P. *Phys. Rev. B* **2010**, *82*, 195206.
- (49) Golovchak, R.; Kozdras, A.; Shpotyuk, O.; Gorecki, Cz.; Kovalskiy, A.; Jain, H. *Phys. Lett. A* **2011**, *375*, 3032–3036.
- (50) Bauchy, M.; Micoulaut, M. *J. Non-Cryst. Solids* **2011**, *357*, 2530–2537.
- (51) Smedskjaer, M. M.; Mauro, J. C.; Sen, S.; Deubener, J.; Yue, Y. Z. *J. Chem. Phys.* **2010**, *133*, 154509.
- (52) Naumis, G. G. *J. Non-Cryst. Solids* **2006**, *352*, 4865–4870.
- (53) Adam, G.; Gibbs, J. H. *J. Chem. Phys.* **1965**, *43*, 139–146.
- (54) Mauro, J. C.; Yue, Y. Z.; Ellison, A. J.; Gupta, P. K.; Allan, D. C. *Proc. Natl. Acad. Sci. U.S.A.* **2009**, *106*, 19780–19784.
- (55) Greaves, G. N. *J. Non-Cryst. Solids* **1985**, *71*, 203–217.
- (56) Greaves, G. N.; Sen, S. *Adv. Phys.* **2007**, *56*, 1–166.
- (57) Jellison, G. E.; Panek, L. W.; Bray, P. J.; Rouse, G. B. *J. Chem. Phys.* **1977**, *66*, 802–812.
- (58) Micoulaut, M.; Kerner, R.; dos Santos-Loff, D. M. *J. Phys.: Condens. Matter* **1995**, *7*, 8035–8052.
- (59) Youngman, R. E.; Haubrich, S. T.; Zwanziger, J. W.; Janicke, M. T.; Chmelka, B. F. *Science* **1995**, *269*, 1416–1420.
- (60) Youngman, R. E.; Zwanziger, J. W. *J. Non-Cryst. Solids* **1994**, *168*, 293–297.
- (61) Gupta, P. K. In *Proceedings of the International Congress on Glass*; New Delhi, 1986.
- (62) Furukawa, T.; White, W. B. *J. Mater. Sci.* **1981**, *16*, 2689–2700.
- (63) Bunker, B. C.; Tallant, D. R.; Kirkpatrick, R. J.; Turner, G. L. *Phys. Chem. Glasses* **1990**, *31*, 30–40.
- (64) Martin, S. W.; Mackenzie, J. W.; Bhatnagar, A.; Bhowmik, S.; Feller, S. A. *Phys. Chem. Glasses* **1995**, *36*, 82–88.
- (65) Lee, S. K.; Musgrave, C. B.; Zhao, P.; Stebbins, J. F. *J. Phys. Chem. B* **2001**, *105*, 12583–12595.
- (66) Massiot, D.; Fayon, F.; Capron, M.; King, I.; Le Calvé, S.; Alonso, B.; Durand, J. O.; Bujoli, B.; Gan, Z.; Hoatson, G. *Magn. Reson. Chem.* **2002**, *40*, 70–76.
- (67) Yue, Y. Z. *J. Non-Cryst. Solids* **2008**, *354*, 1112–1118.
- (68) Moynihan, C. T.; Lee, S. K.; Tatsumisago, M.; Minami, T. *Thermochim. Acta* **1996**, *280*, 153–162.
- (69) Angell, C. A. *Science* **1995**, *267*, 1924–1935.
- (70) Martinez, L.-M.; Angell, C. A. *Nature* **2001**, *410*, 663–667.
- (71) Huang, D. H.; McKenna, G. B. *J. Chem. Phys.* **2001**, *114*, 5621–5630.
- (72) Roland, C. M.; Santangelo, P. G.; Robertson, C. G.; Ngai, K. L. *J. Chem. Phys.* **2003**, *118*, 10351–10352.
- (73) Wang, L. M.; Angell, C. A.; Richert, R. *J. Chem. Phys.* **2006**, *125*, 074505.
- (74) Mauro, J. C.; Loucks, R. J.; Sen, S. *J. Chem. Phys.* **2010**, *133*, 164503.
- (75) Palmer, R. G. *Adv. Phys.* **1982**, *31*, 669–736.
- (76) Gupta, P. K.; Mauro, J. C. *J. Chem. Phys.* **2007**, *126*, 224504.
- (77) Mauro, J. C.; Gupta, P. K.; Loucks, R. J. *J. Chem. Phys.* **2007**, *126*, 184511.

- (78) Mauro, J. C.; Loucks, R. J.; Gupta, P. K. *J. Phys. Chem. A* **2007**, *111*, 7957–7965.
- (79) Potuzak, M.; Mauro, J. C.; Kiczinski, T. J.; Ellison, A. J.; Allan, D. C. *J. Chem. Phys.* **2010**, *133*, 091102.
- (80) Corezzi, S.; Comez, L.; Fioretto, D. *Eur. Phys. J. E* **2004**, *14*, 143–147.
- (81) Araujo, R. J.; Mauro, J. C. *J. Am. Ceram. Soc.* **2010**, *93*, 1026–1031.
- (82) Greenblatt, S.; Bray, P. J. *Phys. Chem. Glasses* **1967**, *8*, 190–193.
- (83) Araujo, R. J. *J. Non-Cryst. Solids* **1980**, *42*, 209–229.
- (84) Mauro, J. C.; Loucks, R. J.; Gupta, P. K. *J. Am. Ceram. Soc.* **2009**, *92*, 75–86.
- (85) Araujo, R. J. *J. Non-Cryst. Solids* **1983**, *58*, 201–208.
- (86) Araujo, R. J. *J. Non-Cryst. Solids* **1986**, *81*, 251–254.
- (87) Bray, P. J.; Mulkern, R. V.; Holupka, E. J. *J. Non-Cryst. Solids* **1985**, *75*, 37–43.
- (88) Mozzi, R. L.; Warren, B. E. *J. Appl. Crystallogr.* **1970**, *3*, 251–257.
- (89) Donohoe, L. M.; Shelby, J. E. *Phys. Chem. Glasses: Eur. J. Glass Sci. Technol. B* **2006**, *47*, 16–21.
- (90) Vilgis, T. A. *Phys. Rev. B* **1993**, *47*, 2882–2885.
- (91) Angell, C. A.; Ngai, K. L.; McKenna, G. B.; McMillan, P. F.; Martin, S. W. *J. Appl. Phys.* **2000**, *88*, 3113–3157.
- (92) Novikov, V. N.; Sokolov, A. P. *Nature* **2004**, *431*, 961–963.
- (93) Dudowicz, J.; Freed, K. F.; Douglas, J. F. *J. Phys. Chem. B* **2005**, *109*, 21350–21356.
- (94) Smedskjaer, M. M.; Mauro, J. C.; Yue, Y. Z. *J. Chem. Phys.* **2009**, *131*, 244514.
- (95) Peter, K. W. *J. Non-Cryst. Solids* **1970**, *5*, 103–115.
- (96) Arora, A.; Marshall, D. B.; Lawn, B. R. *J. Non-Cryst. Solids* **1979**, *31*, 415.
- (97) Yoshida, S.; Sanglebouef, J.-C.; Rouxel, T. *J. Mater. Res.* **2005**, *20*, 3404–3412.
- (98) Yoshida, S.; Hayashi, Y.; Konno, A.; Sugawara, T.; Miura, Y.; Matsuoka, J. *Phys. Chem. Glasses: Eur. J. Glass Sci. Technol. B* **2009**, *50*, 63–70.
- (99) Kato, Y.; Yamazaki, H.; Kubo, Y.; Yoshida, S.; Matsuoka, J.; Akai, T. *J. Ceram. Soc. Jpn.* **2010**, *118*, 792–798.
- (100) Skuja, L.; Hirano, M.; Hosono, H.; Kajihara, K. *Phys. Status Solidi C* **2005**, *2*, 15–24.
- (101) Pacchioni, G.; Skuja, L.; Griscom, D. L. *Defects in SiO<sub>2</sub> and Related Dielectrics: Science and Technology*; NATO Science Series II: Mathematics, Physics and Chemistry; Kluwer Academic: Dordrecht, Germany, 2000.
- (102) Hetherington, G.; Jack, K. H.; Kennedy, J. C. *Phys. Chem. Glasses* **1964**, *5*, 130–136.
- (103) Brückner, R. *J. Non-Cryst. Solids* **1971**, *5*, 177–216.
- (104) Toplis, M. J. *Am. Mineral.* **1998**, *83*, 480–490.
- (105) Du, L. S.; Allwardt, J. R.; Schmidt, B. C.; Stebbins, J. F. *J. Non-Cryst. Solids* **2004**, *337*, 196–200.
- (106) Wondraczek, L.; Sen, S.; Behrens, H.; Youngman, R. E. *Phys. Rev. B* **2007**, *76*, 014202.
- (107) Wu, J. S.; Deubener, J.; Stebbins, J. F.; Grygarova, L.; Behrens, H.; Wondraczek, L.; Yue, Y. Z. *J. Chem. Phys.* **2009**, *131*, 104504.
- (108) Reibstein, S.; Wondraczek, L.; de Ligny, D.; Krolikowski, S.; Sirotkin, S.; Simon, J.-P.; Martinez, V.; Champagnon, B. *J. Chem. Phys.* **2011**, *134*, 204502.
- (109) Yue, Y. Z.; Christiansen, J.; de, C.; Jensen, S. L. *Chem. Phys. Lett.* **2002**, *357*, 20–24.
- (110) Wu, J. S.; Stebbins, J. F. *J. Non-Cryst. Solids* **2010**, *356*, 2097–2108.
- (111) Sen, S.; Topping, T.; Yu, P.; Youngman, R. E. *Phys. Rev. B* **2007**, *75*, 094203.